TRIBHUVAN UNIVERSITY

INSTITUTE OF ENGINEERING

PULCHOWK CAMPUS

THESIS NO: M-111-MSMDE-2024-2026

WALL-MODELED LARGE EDDY SIMULATION STUDY OF SINUSOIDAL TRAILING EDGE IMPACT ON REVERSE FLOW IN HIGH-SPEED ROTORCRAFT

by

Biwash Karki

A THESIS SUBMITTED TO THE DEPARTMENT OF MECHANICAL AND AEROSPACE ENGINEERING IN PARTIAL FULFILLMENT OF THE REQUIREMENTS FOR THE DEGREE OF MASTERS OF SCIENCE IN MECHANICAL SYSTEMS DESIGN AND ENGINEERING

DEPARTMENT OF MECHANICAL AND AEROSPACE ENGINEERING

LALITPUR, NEPAL

April, 2026

COPYRIGHT

TRIBHUVAN UNIVERSITY

INSTITUTE OF ENGINEERING

PULCHOWK CAMPUS

DEPARTMENT OF MECHANICAL AND AEROSPACE ENGINEERING

The undersigned certify that they have read, and recommended to the Institute of Engineering for acceptance, a thesis entitled " WALL-MODELED LARGE EDDY SIMULATION STUDY OF SINUSOIDAL TRAILING EDGE IMPACT ON REVERSE FLOW IN HIGH-SPEED ROTORCRAFT" submitted by Biwash Karki in partial fulfillment of the requirements for the degree of Master in Mechanical System Design and Engineering.

Supervisor, Sudip Bhattarai
Assistant Professor
Department of Mechanical and Aerospace Engineering

Supervisor, Kamal Darlami,
Assistant Professor
Department of Mechanical and Aerospace Engineering

Bimal Bhattarai
External Examiner
Nepal Airlines Corporation(NAC)

त्रिभुवन विश्वविद्यालय
इन्जिनियरिङ्ग अध्ययन संस्थान
मेकानिकल तथा एरोस्पेस इन्जिनियरिङ्ग विभाग
पुल्चोक क्याम्पस

Committee Chairperson, Sudip Bhattarai
Head of the Department
Department of Mechanical and Aerospace Engineering

Date: 2026/04/24

ABSTRACT

In rotorcraft aerodynamics, reverse flow in the retreating blade is a critical challenge at high advance ratios. This limits the maximum achievable forward speed. During reverse flow, the trailing edge becomes the aerodynamic leading edge. There is early flow separation. In this numerical study, reverse flow over two (one straight trailing edge and other with a sinusoidal trailing edge) NACA 0015 blades are compared. The sinusoidal trailing edge have amplitude equal to 10% of the chord length and wavelength equal to 10% of the chord length, The study is conducted for a chord-based Reynolds number of 1.35×10^5 using OpenFOAM and ParaView visualization. Results show that the flow separation is completely mitigated over the modified blades at the static pitch angles where the baseline was fully separated. The sinusoidal trailing edges are thus evaluated to be highly effective in controlling and mitigating the adverse effects of reverse flow.

ACKNOWLEDGEMENTS

I would like to thank Assistant professor Kamal Darlami for recommending me this topic. I would like to express my sincere gratitude to Assistant professor Sudip Bhattarai for constantly helping me throughout this work. This research work couldn't been in this place without my supervisors.

I would like to thank all my professors who were there in different aspects of my master's journey. I would like to thank my MSMDE senior Sandeep Gawayali (MSMDE078) for guiding me in the different phases of this project. I would also like to thank Nischal poudel (Aero075), Prativa Bhandari (Aero075) for making me familiar with department in the early days. I would also like to thank Priyanka Sinha for her insights on validation approach. I would also like to thank all my classmates and non-teaching staffs of the DMAE.

Lastly, I want to express my gratitude to everyone who has assisted me in this thesis work in different ways.

TABLE OF CONTENTS

LIST OF TABLES

LIST OF FIGURES

LIST OF SYMBOLS

$\overline{u_\iota}$	Filtered velocity
$\bar{p}$	Filtered Pressure
$\overline{S_{\iota J}}$	Filtered strain-rate tensor
τ^{sgs}	SGS stress tensor
ϑ_{sgs}	Filtered kinematic viscosity
ϑ	Kinematic viscosity
$\frac{\partial}{\partial t}$	Temporal derivative
∂_i	Displacement in x-direction
∂_j	Displacement in y-direction

LIST OF ABBREVIATIONS

NACA	National Advisory Committee for Aeronautics
Re	Reynolds Number
C_L	Coefficient of Lift
C_d	Coefficient of drag
AOA	Angle of Attack
WMLES	Wall Modeled Large Eddy Simulation
GCI	Grid Convergence Index
CFD	Computational Fluid Dynamics
ALE	Aerodynamic Leading Edge
ATE	Aerodynamic Trailing Edge
LES	Large Eddy Simulation
DES	Detached Eddy Simulation
DNS	Direct Numerical Simulation
RANS	Reynolds-averaged Navier-Stokes equations
SGS	Sub Grid Scale

CHAPTER ONE: INTRODUCTION

1.1 Background

At high advance ratios, a retreating blade of rotorcraft blade encounters reverse flow near hub (Hiremath, 2019). The retreating blade generated less lift compared to the advancing blade due to reduced relative velocity. Angle of attack of the retreating blade is increased to maintain lift symmetry. However, while increasing the angle of attack, the blade starts to experience stall (Cantrell, n.d.).

In rotor aerodynamics, at high advance ratio reverse flow is a natural phenomenon. It itself is not a problem. The real problem is what reverse flow brings. Flow separation and imbalance of lift are caused by reverse flow (George Jacobellis, 2018). These factors affect the performance of the rotor. Reverse flow in retreating blade is shown in Figure 1.

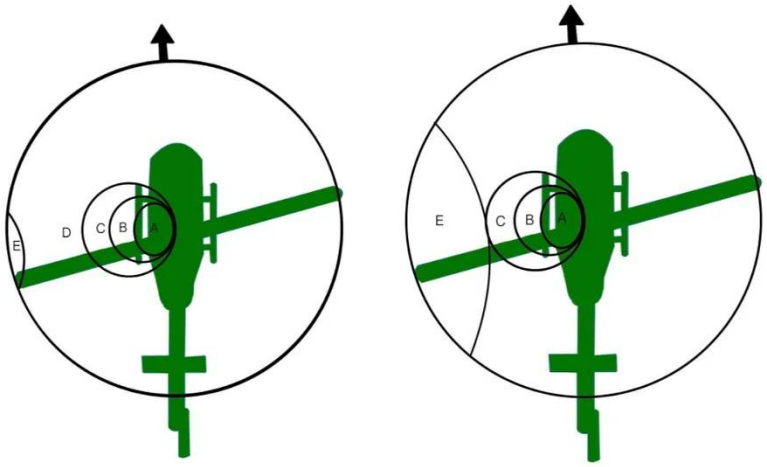

Figure 1: Retreating Blade Stall (Komal, 2025)

The portion A is the regime of reverse flow. The portion B is the regime of negative stall. The portion C is the regime of negative lift. The portion D is the regime of positive lift and the portion E is the regime of positive stall (Komal, 2025). The imbalance in lift generation between retreating blade and advancing blade is shown in Figure 2. This imbalance is compensated by increasing the angle of attack. When critical angle of attack is reached the blade stalls. The blade stalls at the blade tip in the 9 o'clock position and moves inward (Retreating Blade Stall, 2025).

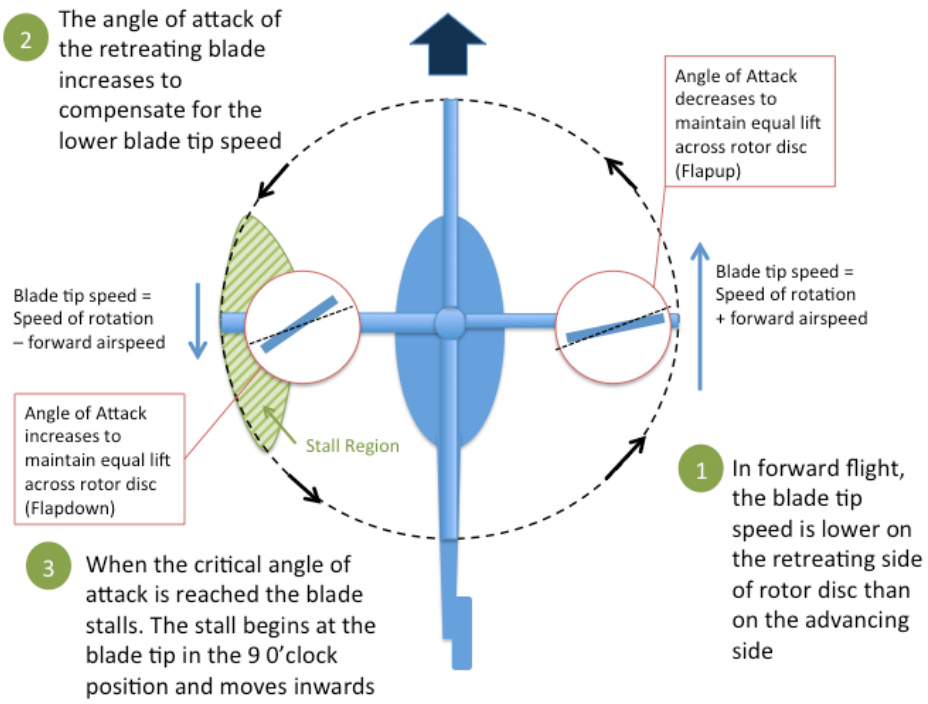

Figure 2: Schematic Explanation of Retreating Blade (Retreating Blade Stall, 2025)

1.2 Statement of the Problem

To mitigate the challenges posed by reverse flow, various techniques have been proposed and are in study. Dynamic pitching is a common practice. Under various flow conditions, passive chamber morphing has shown positive effects in adapting aerodynamic characteristics (Cooper Nelson, 2024). Leading-edge tubercles inspired by humpback whale's fin have been studied for their effects in flow control at stall regions (H. Johari, 2007). Most recently, experimental studies have been investigated the impact of serrated trailing edge on aerodynamic characteristics (Raamesh Balasubramani, 2024). While experimental insights are available, numerical studies remain limited.

In this research, the sinusoidal trailing edge impact is investigated for a rotorcraft blade. A computational study is conducted on OpenFOAM using wall-modeled large eddy simulation. Comparative study is done for baseline and serrated case to evaluate the aerodynamic characteristics.

1.3 Objectives of Research

Main Objective:

To investigate the aerodynamic impact of sinusoidal trailing edges on reverse flow in high-speed rotorcraft using Wall-Modeled Large Eddy Simulation.

Specific Objectives:

1. To implement a WMLES framework for reverse flow simulation over rotorcraft airfoils.
2. To analyze the reverse flow behavior and separation mechanisms at different AOA.
3. To compare the simulation results with available experimental data.

CHAPTER TWO: LITERATURE REVIEW

2.1 Historical Overview and Current Flow Control Techniques in Reverse Flow

Since the early developments in rotorcraft aerodynamics, the phenomenon of reverse on the retreating blade of a helicopter rotor has been studied. At high advance ratios, a significant portion of the retreating rotor blade enters a reverse flow regime, where air flows from the trailing edge toward the leading edge. This results in strong adverse pressure gradients, boundary layer separation, and eventually dynamic stall. The onset of stall typically begins near the outboard section of the blade at 9 o'clock position and progress inward with increasing forward speed (Retreating Blade Stall, 2025).

To address the performance, the various techniques have been explored. Among passive methods, camber morphing airfoils have been developed to adapt the blade dynamically to local flow conditions (Cooper Nelson, 2024). Inspired by humpback whale flippers, the study of sinusoidal tubercles effect in airfoils is actively in research. Leading-edge tubercles inspired by humpback whale's fin as shown in Figure 3 is used for reverse flow mitigation. In Pulchowk Campus, DMAE, recently study was done on leading-edge sinusoidal tubercles which showed the tubercles postponed stall by 6^{o}, increase lift by 17 % and reduce drag by 12% (Bishowdip Khadka, 2025). Among numerous configurations that could be generated by varying wavelength and amplitude, the leading-edge tubercles with an amplitude 3% chord and a wavelength of 20% chord produces more lift than the baseline wing at the pre-stall, stall and post-stall zones.

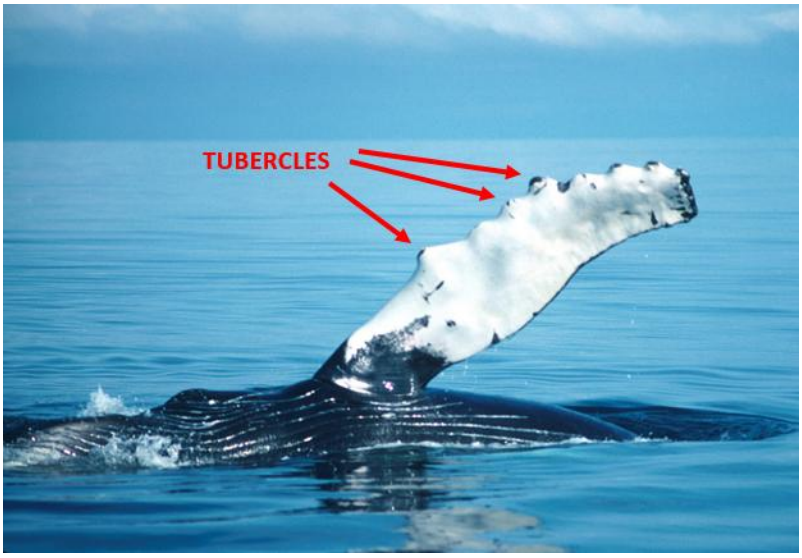

Figure 3:Bumps or Tubercles on whale pectoral fin (BIOMMICRY, 2016)

In rotor aerodynamics, there is reverse flow in retreating blade. Reverse flow is not inherently a problem, it's a natural aerodynamic condition at high advance ratios. The real aerodynamic problem is what reverse flow causes: flow separation, dynamic stall, imbalance of lift and loss of control authority (George Jacobellis, 2018). So, experimental study of trailing-edge sinusoidal tubercles has also been recently done in IIT Kanpur which showed flow remains attached up to 190^0-192^0 AOA (Raamesh Balasubramani, 2024). It was seen that along the sinusoidal crest plane of the modified blade, the flow is completely attached till $\alpha = 190^o$. Flow only separates at $\alpha=192^o$ at 90 % chord location, which moves upstream to 70% chord location at $\alpha=194^o$. At sinusoidal-middle and sinusoidal-trough planes, flow separation occurs at approximately 90 % chord location at $\alpha = 194^0$ (Raamesh Balasubramani, 2024). Apart from experimental study, numerical studies are also there, Marilyn have investigated the aerodynamics of airfoils at high and reverse angles of attack, It was observed that the recently developed hybrid RANS and Large Eddy Simulation(LES) predict the characteristics of airfoils in these angles of attack regimes (Marilyn Smith, Aerodynamics of airfoils at high and reverse angles of attack, 2012). Similarly research on LES with modeled wall-stress have found that wall modeled LES is more accurate than Detached eddy simulation(DES) and LES. By resolving the outer part of the boundary layer, wall modeled LES is more accurate than DES. It is also clear that properly performed wall modeled LES is not computationally cheap, it can be orders of magnitude cheaper than LES, but it is still orders of magnitude more expensive than both DES and RANS (Johan LARSSON, 2016).

2.2 Numerical Approaches and Wall-Modeled Large Eddy Simulation

The turbulent boundary layer is typically is typically divided into:

- Inner layer: Dominated by viscous effects, located very close to wall.
- Outer layer: Dominated by inertial effects and larger eddies.

The peak turbulence kinetic energy occurs around $y^+ \approx 12$ (D. Dupuy, 2019).

LES is a computational fluid dynamics technique to solve turbulent flows. Turbulent flows contain eddies with a range of sizes and energies. LES is good at capturing large turbulent motion but it also needs to resolve the small motions near the wall. Resolving the inner layer, small eddies near the wall becomes extremely computationally expensive as it leads to rapid growth in grid requirements.

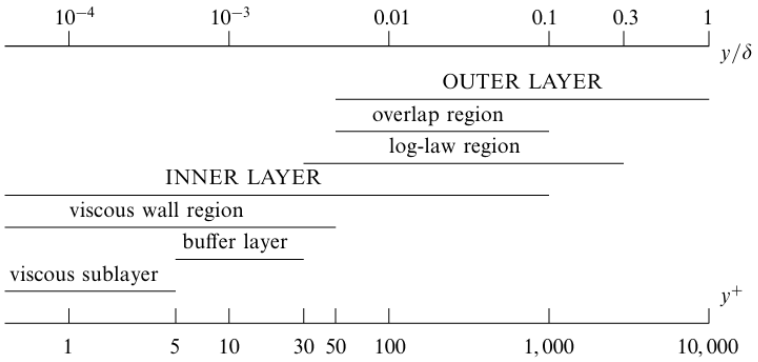

Figure 4: Various wall regions and layers (Pope, 2000)

For flat plate TBL, the required number of grid points N grow roughly as $N \propto Re^{1.85}$ (Xiang IA Yang, 2021). This exponential growth makes wall-resolving LES prohibitively expensive for high Reynolds number flows. So, to overcome this, we model the inner-layer. In doing so, we consider the Kolmogorov turbulence theory shown in Figure 5 which postulates that the small-scale structure of turbulence is statistically homogeneous, isotropic, and independent of the large-scale structure.

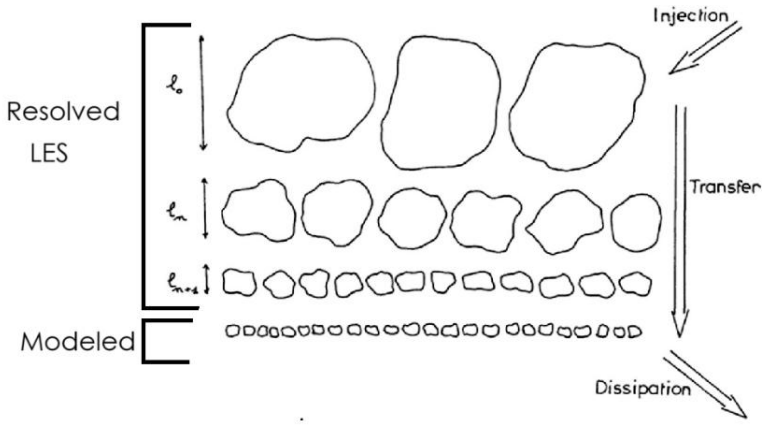

Figure 5: Energy Cascade theory (Ye Zhou, 2019)

This study uses wall-modeled large eddy simulation (WMLES) to investigate the aerodynamic characteristics of the rotor blade under reverse flow conditions. Wall-modeled large eddy simulation is chosen due to it's ability to resolve large-scale turbulent structures while modeling near-wall effects. The wall modeling is the wall stress model and we utilize the open source library libWallModelledLES (Timofey Mukha, 2019). The flow is governed by filtered Navier-Stokes equations:

Continuity equation:

$$\frac{\partial \overline{u_i}}{\partial x_i} = 0 \tag{i}$$

Momentum equation:

$$\frac{\partial \overline{u_i}}{\partial t} + \frac{\partial \overline{u_i}\,\overline{u_j}}{\partial x_j} = -\frac{\partial \bar{p}}{\partial x_i} + \frac{\partial}{\partial x_i}\left(\tau^{sgs} + 2\vartheta \overline{S_{ij}}\right) \quad i = 1, 2, 3 \tag{ii}$$

The strain-rate tensor is defined as:

$$\overline{S_{ij}} = \frac{1}{2}\left(\frac{\partial \overline{u_i}}{\partial x_j} + \frac{\partial \overline{u_j}}{\partial x_i}\right) \tag{iii}$$

and

$$\tau^{sgs} = \overline{u_i}\,\overline{u_j} - \overline{u_i u_j} \tag{iv}$$

is the SGS stress tensor. The SGS stresses are modeled using an eddy-viscosity assumption: $\tau_{ij}^{sgs} = 2\vartheta_{sgs}\overline{S_{ij}}$, which leads to the modified momentum equation:

$$\frac{\partial \overline{u_i}}{\partial t} + \frac{\partial \overline{u_i}\,\overline{u_j}}{\partial x_j} = -\frac{\partial \bar{p}}{\partial x_i} + \frac{\partial}{\partial x_i}\left(2(\vartheta_{sgs} + \vartheta)\overline{S_{ij}}\right) \tag{v}$$

To compute the wall shear stress, the wall model takes the sampled velocity from the coarse grid. The wall model solves a separate algebraic equation (the log-law) to estimate the true velocity gradient at the surface. This computed stress is then enforced in the Navier-Stokes equations by manually overwriting the viscous flux at the wall-adjacent cell faces. Schematic working of wall-stress model is represented in Figure 6.

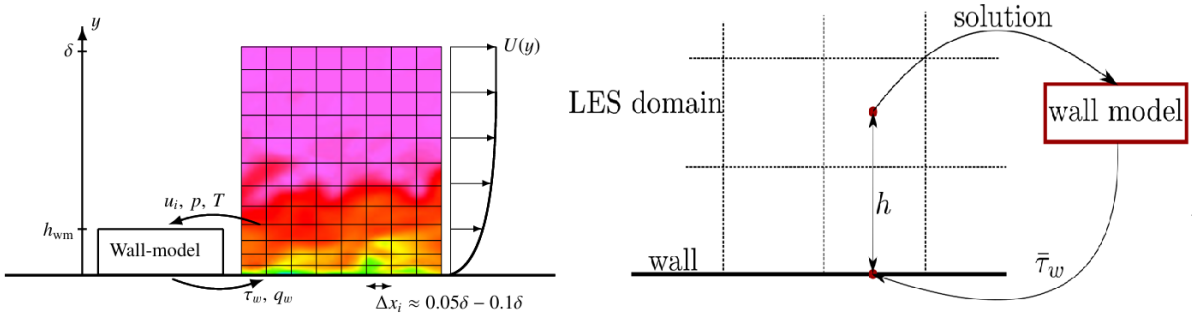

Figure 6: Way of working of wall-stress model (Johan LARSSON, 2016)

$$\overline{\tau_{w,i2}} = (\vartheta + \vartheta_{sgs})\frac{\overline{u_{i,P}}}{\Delta x_2} \tag{vi}$$

The drag force from (vi) ensures that the drag force applied to the momentum equation matches the stress predicted by the Law of the Wall, effectively bridging the coarse grid to the physical surface. The Wall-modeled LES is different from both the original DES and traditional LES. By resolving the outer part of the boundary layer, WMLES has the potential to be much more

accurate than DES. It is also clear that properly performed WMLES is not computationally cheap, it can be orders of magnitude cheaper than LES, but it is still orders of magnitude more expensive than both DES and RANS (Johan LARSSON, 2016).

CHAPTER THREE: RESEARCH METHODOLOGY

The overall methodology of the current study consists of various stages as shown in Figure 7. The study begins with a comprehensive literature review to develop understanding of reverse flow aerodynamics in rotorcraft blades. Particularly during high advance ratios in the region near hub section of retreating blade. Flow separation mechanisms is studied and importance of separation point and influence of vortex nature in reverse is noted. Additionally, existing flow control strategies are reviewed, including passive techniques like bio-inspired sinusoidal leading-edge modifications, which have shown potential in delaying flow separation and improving aerodynamic characteristics. Simultaneously, various modeling approaches are studied to determine an approximate simulation strategy. These include Unsteady RANS, Detached eddy simulation, Wall modeled large eddy simulation, large eddy simulation and Direct numerical simulation. Based on study WMLES is chosen for this study. WMLES seems to be balance between computational and accuracy for separated flows. Then a simulation framework is created. The Wall-Modeled Large Eddy Simulation (WMLES) setup is based on the approach proposed by Timofey Mukha (Timofey Mukha, 2019).

The computational simulations are carried out using OpenFOAM v2412. It is an open-source platform widely used for computational fluid dynamics applications. PimpleFoam solver was used where turbulence model is wall-stress modeling. Here, filtered Navier-Stokes equations are solved for region above log layer and modeled below the log layer. The sub-grid scale turbulence model is wall-adapting local eddy viscosity model. The eddy viscosity assumption is worked with the law of the wall to get the modeled sub grid scale kinematic viscosity.

For the geometric modeling, Fusion 360 is used as it as simpler modeling approach for serrations in trailing edge. The computational mesh is generated using ANSYS Fluent meshing also known as mosaic meshing (poly-hex core). This meshing approach was chosen as it is easier to mesh the boundary layers and outer layers separately. The wingspan is considered 20% of chord length to see quasi 2D effects (W. Yang, 2012). Following mesh generation, mesh validation and solver validation is carried out. Firstly, solver validation is done for a simpler domain, flat plate where meshing is done by GMSH which is efficient for meshing regular shapes. The validation is done against the available DNS data. Then, mesh validation is done and computational setup is verified. After this, simulations are performed for both baseline and serrated airfoil for different angles of attack. The simulations results is post processed in MATLAB and visualization is done in ParaView. Normalized velocity contours with time-averaged in plane velocity streamlines are used for visualization of circulation

regions. The numerical findings are then compared with available experimental data. If undesirable and unanswerable results are observed, necessary revisions are done in WMLES setup (meshing, openFOAM case file). Lastly, after completion of work, the documentation is carried out.

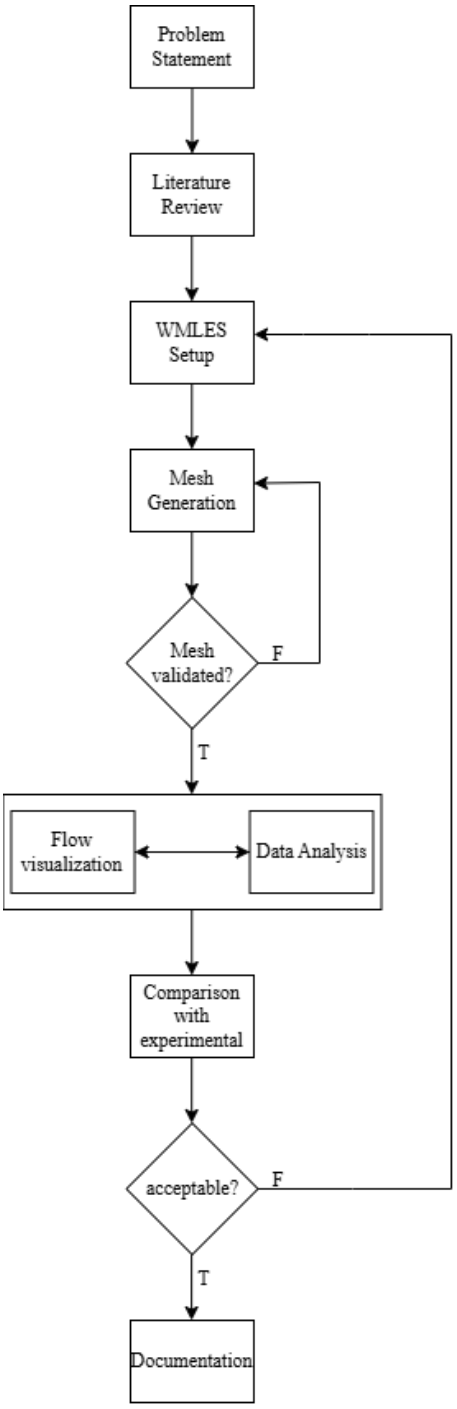

Figure 7: Conceptual Framework

CHAPTER FOUR: COMPUTATIONAL WORK

4.1 Solver Validation

The numerical solver is validated using a benchmark case of Zero-pressure-gradient turbulent boundary layer developing over a flat plate. This is a widely accepted test case for assessing turbulence modeling approaches. The configuration of the validated case is illustrated in Figure 8, showing the computational domain, boundary conditions, and flow development region.

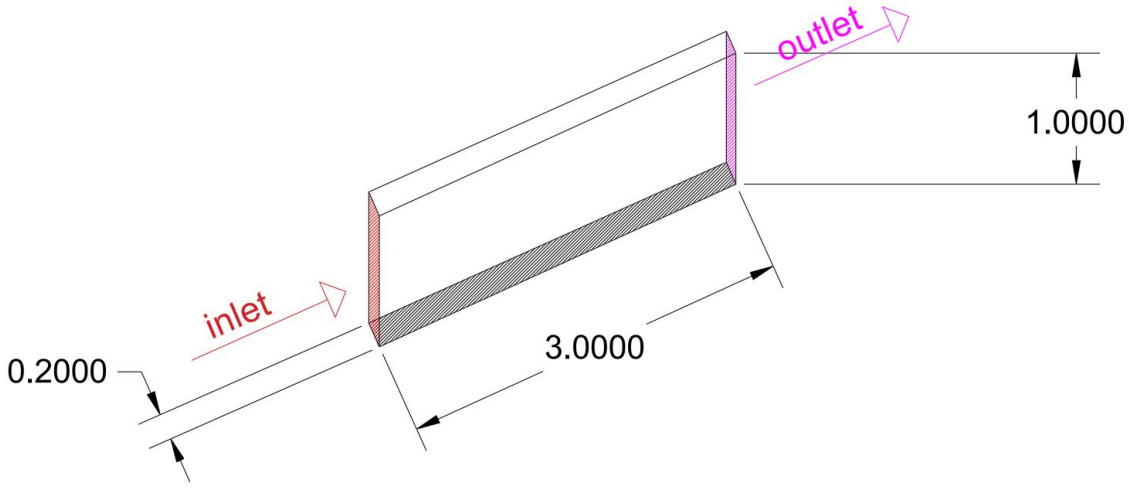

Figure 8: Case Overview

A simple case overview is shown Figure 8, where free stream velocity is 20.4m/s and kinematic viscosity is 1.65e-5m^2/s. The simulation results are compared against high-fidelity Direct Numerical Simulation (DNS) data made publicly available by the KTH Royal Institute of Technology (Örlü, 2010). This dataset is well-established in the literature and serves as a reliable reference for evaluating the accuracy of wall-modeled large eddy simulation (WMLES). To facilitate a clearer and more consistent comparison between the present results and the DNS data, a curve-fitting approach is employed to smooth the numerical data and highlight the underlying trends. As shown in Figure 12 the WMLES predicted 87% of DNS magnitude which is good agreement with the reference DNS data across the boundary layer profile. In particular, the predicted skin-friction coefficient is captured with reasonable accuracy, indicating that the wall-modeling approach is effectively representing near-wall turbulence behavior. Minor deviations can be observed in certain regions, which may be attributed to modeling assumptions and grid resolution limitations; however, the overall trend and magnitude remain consistent with the DNS results. Meshing approach for solver validation is shown in Figure 9 and Figure 10.

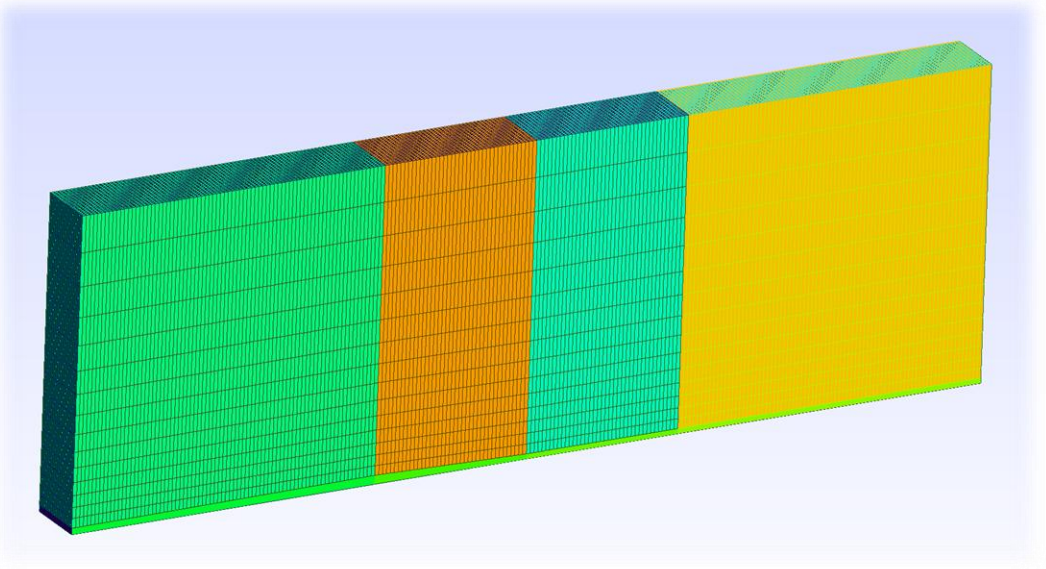

Figure 9:Meshing

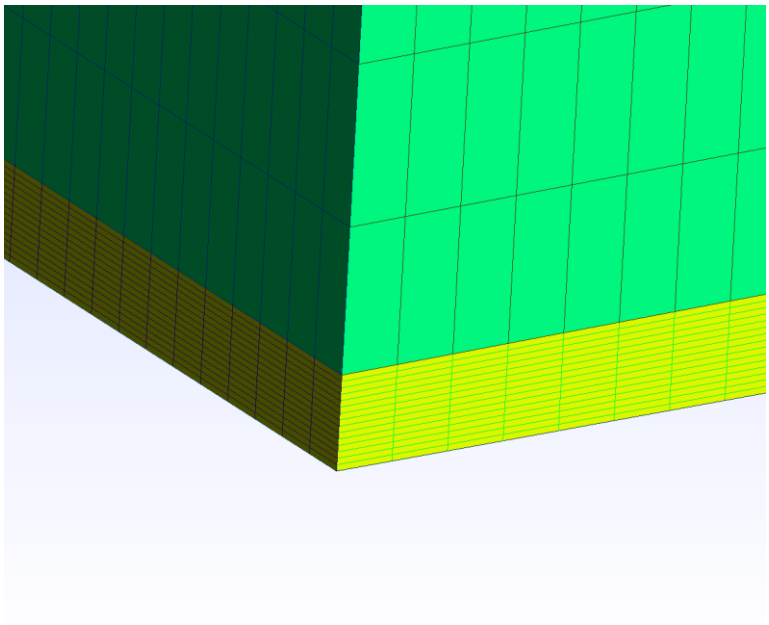

Figure 10:Enlarged Meshing

Though WMLES do not need super refined mesh as RANS-LES Hybrid. We need to adjust the sampling cells within the range of log-layer. So meshing was done accordingly. For this validation meshing was done using GMSH software an open source software.

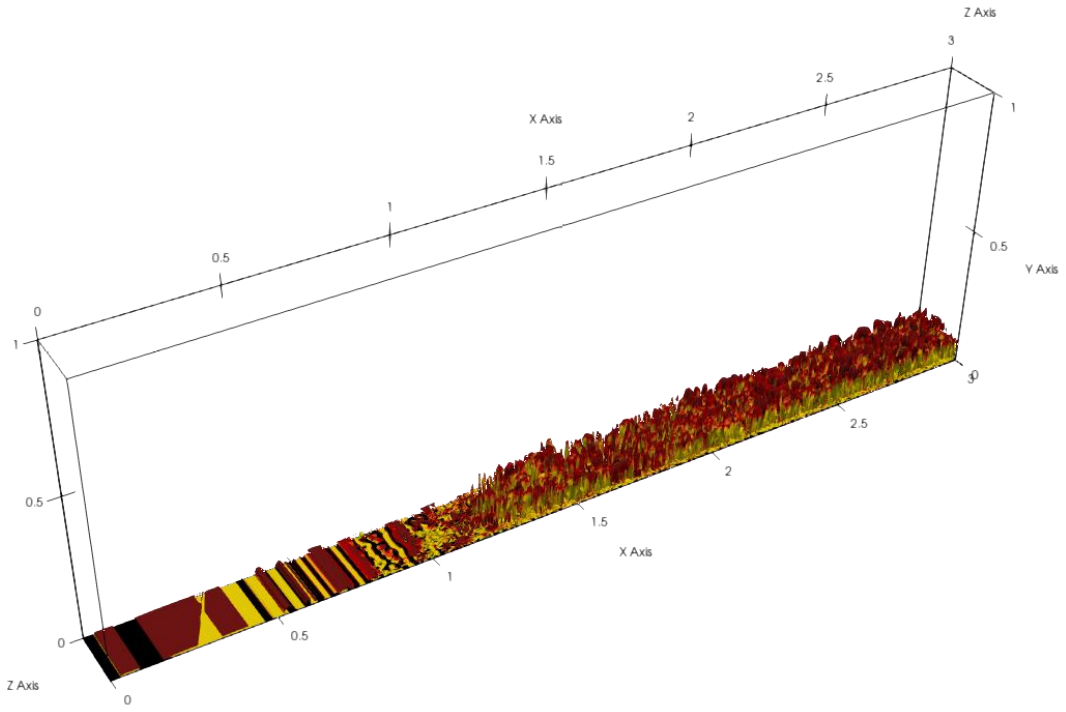

Figure 11: Q- Criterion

Q-criterion is plotted in Figure 11 to help visualize vertical structures in fluid flow. It also gives idea about where flow transitioned from laminar to turbulent.

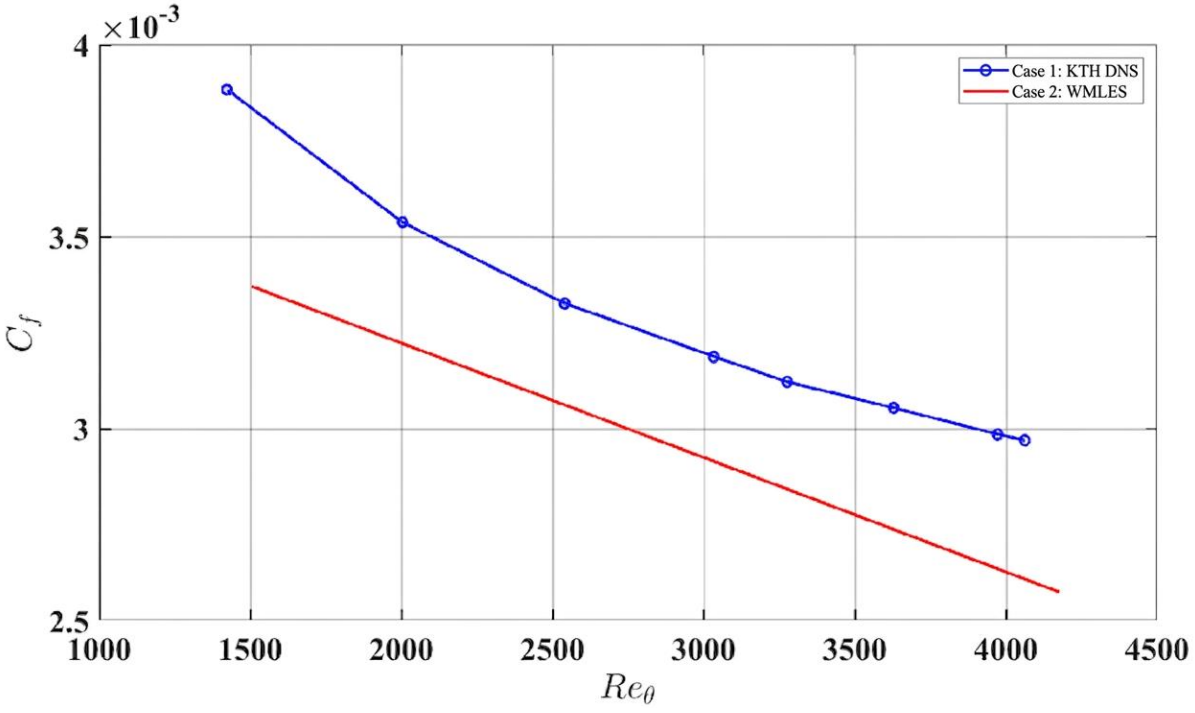

Figure 12:KTH DNS vs Our WMLES

4.2 Geometry

The NACA 0015 airfoil is selected as the baseline geometry. The computational domain will extend up to 100 times the chord length to minimize boundary effects. The span of the wing is 20% of the chord length (Xiang IA Yang, 2021). This is to incorporate the quasi-2D effects. Two geometries is analyzed: one with a conventional straight trailing edge as in Figure 13, and the other featuring a sinusoidal trailing edge modification as in Figure 14.

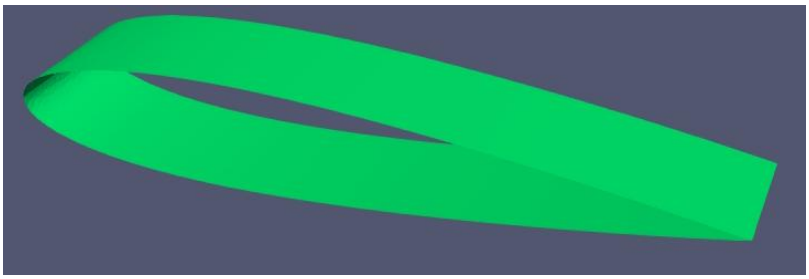

Figure 13:Baseline geometry

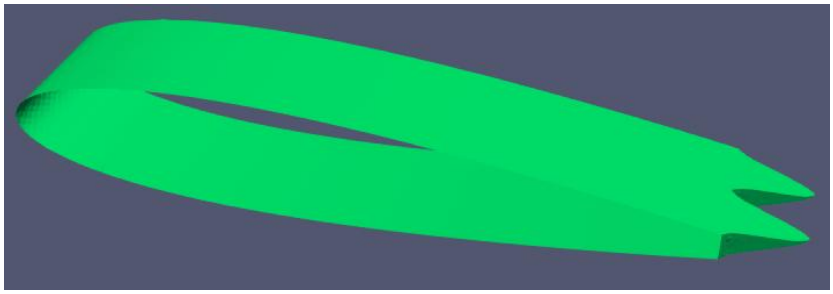

Figure 14:Serrated geometry

Table 1: Serration Metrics

Serrated Geometry	Amplitude	Wavelength
	10 % of Chord length	10% of Chord length

4.3 Mesh Independence Study

A structured mesh is generated using ANSYS Fluent Meshing. The grid is refined near the wall to capture boundary layer effects. The grid is coarser farther from the wall surface. This is to reduce the computational cost without losing the boundary layer effects. Wall stress modeling is applied so that the sampling is within the logarithmic layer $30 < y^{+} < 500$. Second off-wall cell in the meshes as we studied.

A standard practice, a study of three levels of grid resolution is conducted. Coefficient of drag is compared for coarse, medium and fine mesh for studying sensitivity. Richardson extrapolated solution is calculated and variance is studied for each mesh. The cell count growth is $\sqrt{2}$. Coefficient of Drag is compared for different meshes at AOA 170. Relative Error and difference is studied in Table 2.

Table 2: Grid Convergence Study

Mesh	Number of Cells	Coefficient of drag	Difference	Relative Error
Coarse	41192	0.1425		
Medium	58315	0.1285	0.014	0.1089
Fine	83306	0.1261	0.0024	0.019

The exact coefficient of Drag value obtained from Richardson Extrapolation is 0.12553. Also, the order of convergence obtained was 5.088. The variance from Richardson Extrapolation Solution is tabulated in Table 3.

Table 3: Grid Convergence Study Richardson Extrapolation Solution

Mesh	Number of Cells	Coefficient of drag	Difference from Richardson solution	Percentage Error
Coarse	41192	0.1425	0.01697	13.518%
Medium	58315	0.1285	0.00297	2.36%
Fine	83306	0.1261	0.00057	0.454%

To futher quantify the grid independence, the Grid Convergence Index (GCI1 is calculated. The Grid Convergence Index between the coarse-medium and medium-fine is tabulated in Table 4. The lower Grid Convergence Index value of 0.49% between the medium and fine mesh indicates that the medium mesh solution is effectively grid- independent. Grid convergence behaviour is illustrated in Figure 15.

Table 4: Grid Convergence Index

Mesh	G.C.I.
Coaarse-Medium	0.0281
Medium-Fine	0.0049

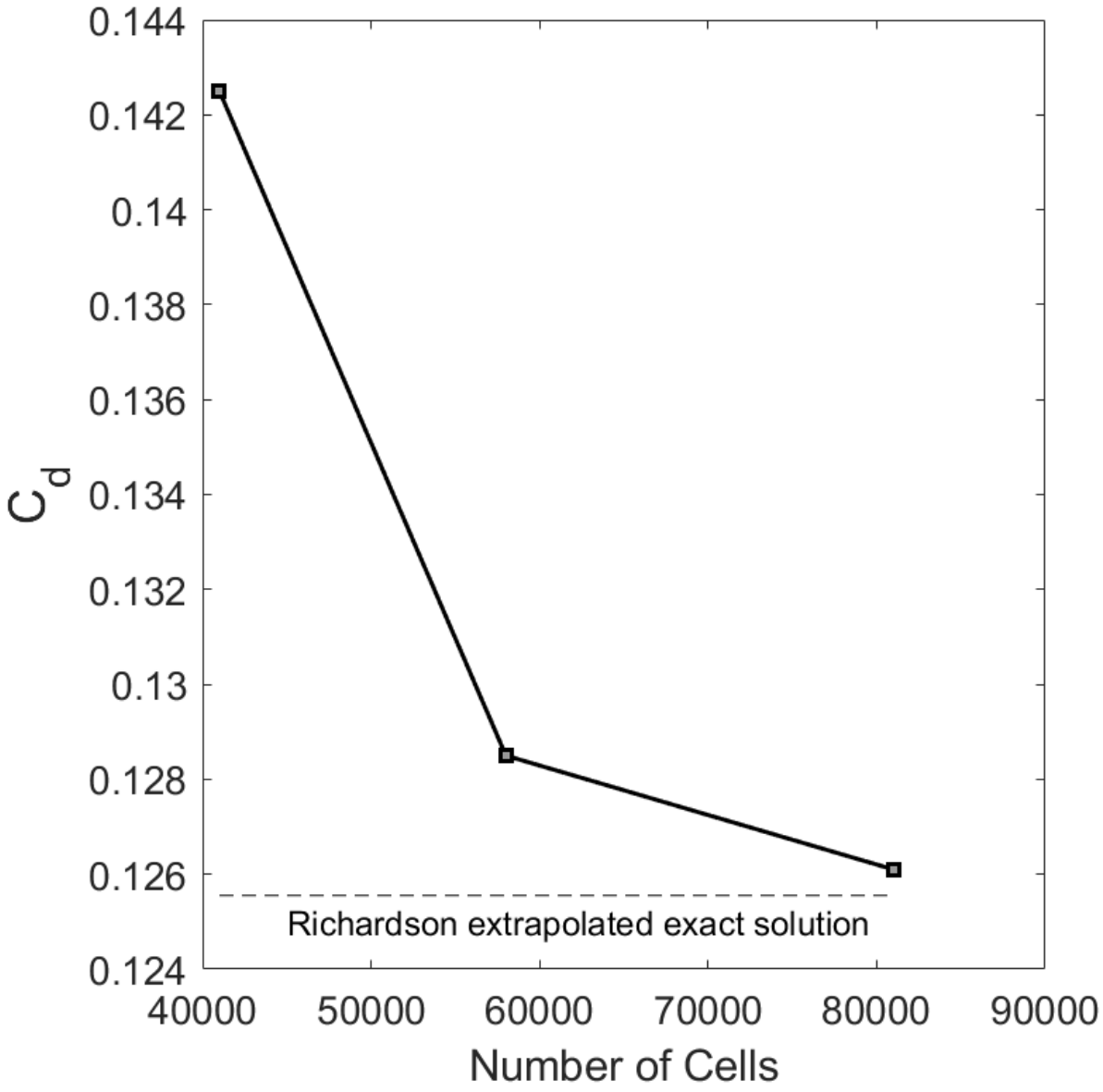

Figure 15: Grid Convergence Study with Richardson Extrapolation solution

The mesh quality was evaluated using the checkMesh utility in OpenFOAM. The primary metrics targeted are the Maximum Aspect Ratio and Maximum Skewness. The values are tabulated in Table 5.

Table 5: Max. aspect ratio Max. skewness of meshes

Mesh	Max. aspect ratio	Max. skewness
Coarse	5.087	2.70
Medium	6.59	2.97
Fine	6.689	2.37

The maximum skewness values remain within the computational range for the selected pressure-velocity coupling. While the aspect ratio increases slightly with a refinement which is due to an increase in inflation layers to maintain y^+. Based on the Grid convergence Index(GCI) of 0.49% and the stable mesh metrics, the medium mesh was chosen. This mesh ensures that the solution is independent of spatial discretization. The selected mesh meshing configuration is shown in Figure 16 and near-wall refinement is shown in Figure 17.

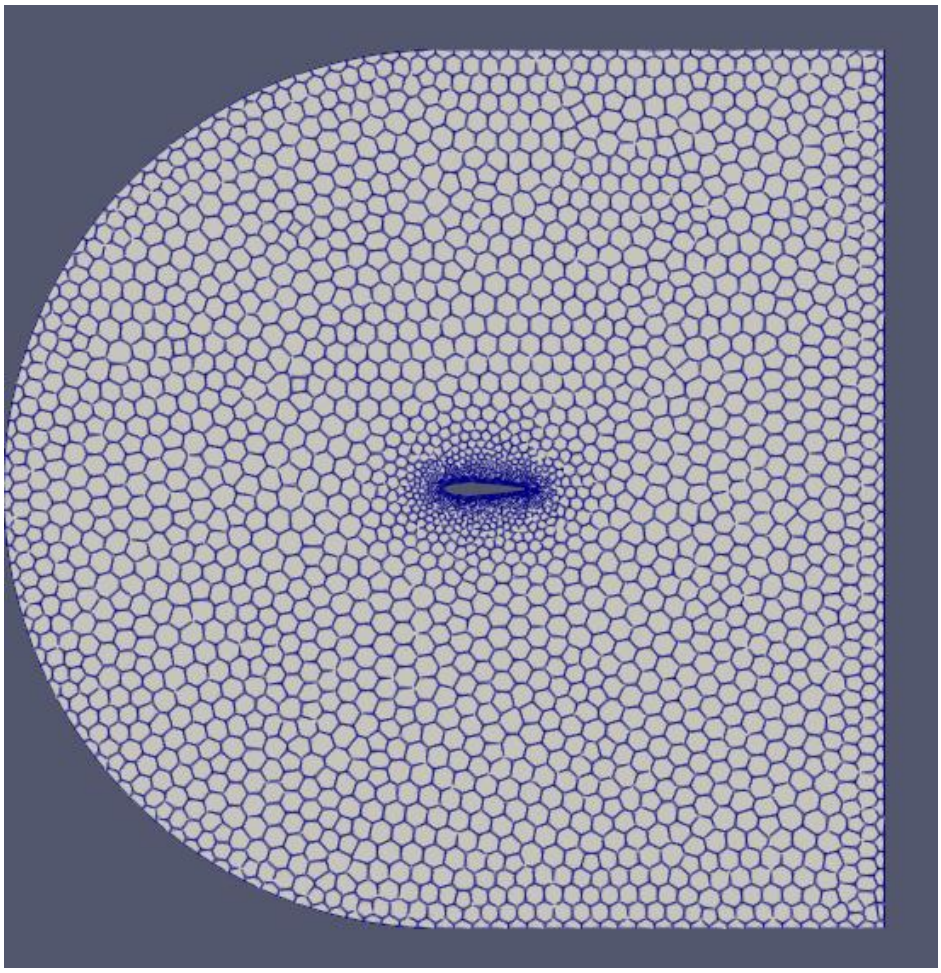

Figure 16:Converged Mesh

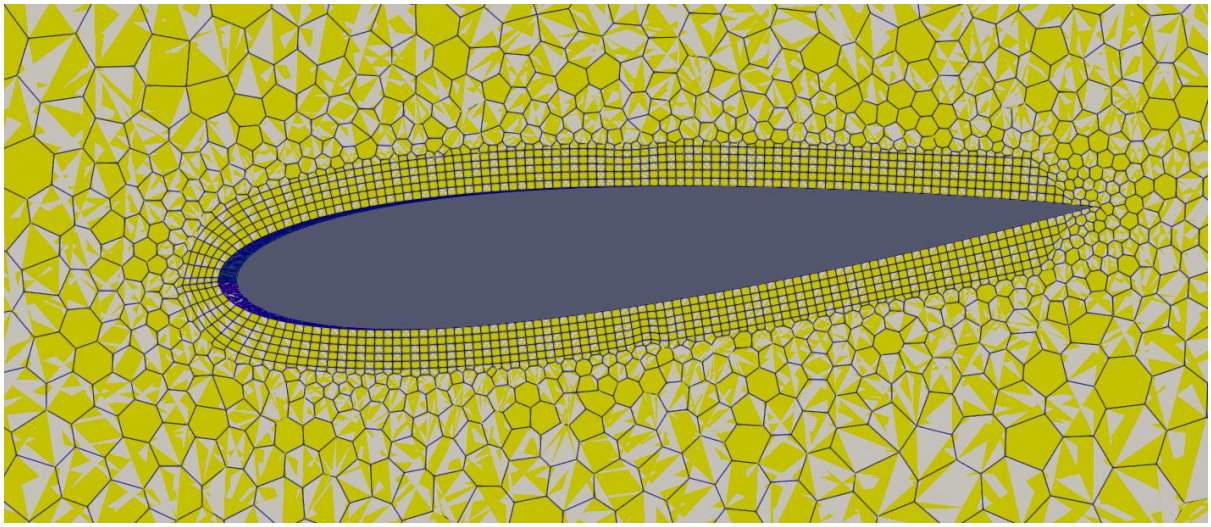

Figure 17:Converged Mesh (Near wall meshing)

4.4 Simulation Setup

The illustration of the simulation configuration, including the airfoil, inlet, outlet, and fluid domain in shown in Figure 18. The simulations are conducted at a chord-based Reynolds number of 1.35×10^5, with a free-stream velocity of 20m/s.

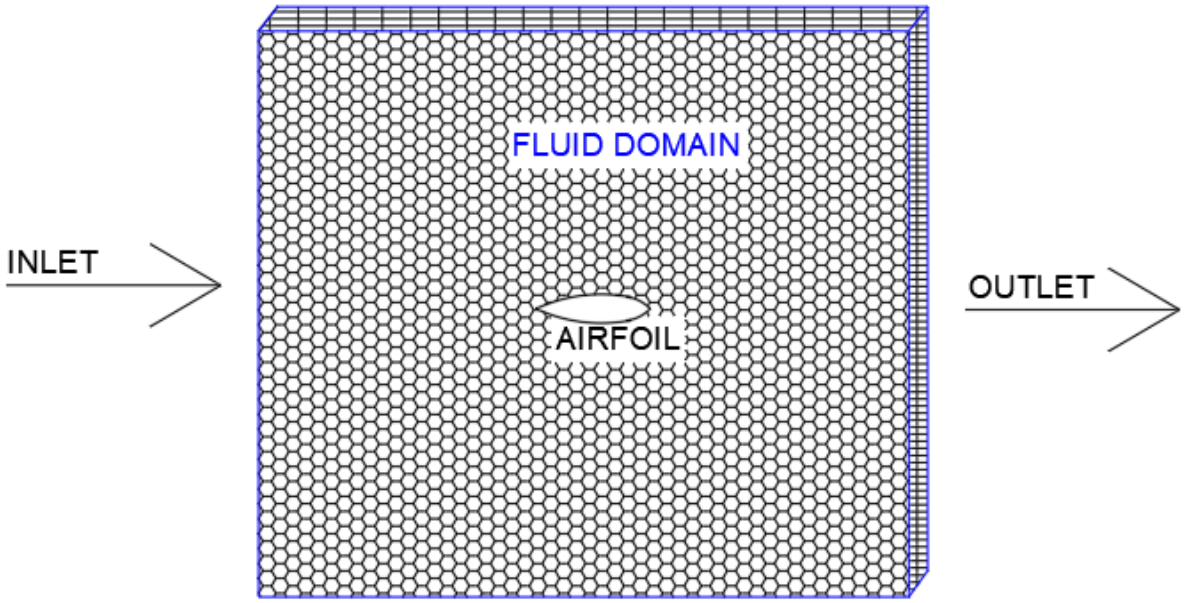

Figure 18: Simulation Setup

The conditions used for the reverse flow study are shown in Table 6. Wall modeling is applied such that the near-wall resolution lies within the logarithmic region. The region below the log region is modeled. The Reynolds number and freestream velocity are selected to lie within the

range of experimentally investigated reverse flow regimes, ensuring physical relevance to retreating blade aerodynamics.

Table 6: Test Conditions

Chord length	0.1m
Free Stream Velocity	20 m/sec
Re_c	135135.135
Wall-modeled	Below log layer
Wing Span	0.02m
Front & Back Face BC	Cyclic Boundary

CHAPTER FIVE: RESULTS AND DISCUSSION

5.1 Lift Coefficient

The overall absolute values of the lift coefficients for the baseline and serrated configuration is tabulated in Table 7 and presented in Figure 19. The lift curve slope demonstrates a notable improvement in aerodynamic performance. Negative lift in reverse flow is undesirable, and the baseline case exhibits relatively high values of negative lift. In contrast, the serrated configuration shows a substantial reduction in lift magnitude. For the Baseline blade, the lift begins to deviate between 176 ° and 164 °. For the baseline blade, the linear slope, plateauing around 172 º and rising again from 166 º. For the serrated blade, the lift increases steadily up to 166 º, behind which a slight reduction in coefficient values is seen. The baseline airfoil does not produce any lift until a certain critical angle, which is 176 º or 4 º. Beyond 176 º there is sharp increase in the coefficient of lift until 170 º. After 170 º a plateau is formed until a certain spike at 164 º. The baseline configuration shows high sensitivity after certain angles, 176 º and 164 º in particular. In contrast to the baseline, the serrated airfoil demonstrates a linear pattern, as if the flow is not flowing from the trailing edge to the leading edge. This could be because the serrations act as vortex generators. The serrations force the air to spin into a stream-wise vortex. These vertices pull energy from the free-stream down towards the surface. This helps flow remain attached to the airfoil or reattach sooner than it would on a straight sharp edge. This indicates the presence of a favorable pressure gradient. In baseline, the flow separates earlier unlike traditional LE where flow wraps around smooth curved surface. In traditional LE to follow the curve the fluid accelerates which lowers pressure. This creates powerful suction right at the front of the wing. This suction peak pulls the wing up generating most of the lift. For our baseline our ALE is flat surface, the air moving at the high speed cannot wrap around it shoots. Unlike traditional LE, no suction pressure is generated so enough deviations (AOA) have to be reached before the flow on the upper side behaves differently enough from the lower side to produce measurable lift coefficient. The coefficient of lift for the serrated airfoil is higher at lower AOA (below 174 º), whereas the baseline exhibits a higher value of the coefficient of lift at higher AOA (above 176 º). The peak value $C_{L_{max}}$ for the serrated airfoil is also compared to the baseline. There is an overall reduction in peak value by approximately 30%.

Table 7: Coefficient of Lift : Baseline vs Serrated

AOA	Baseline	Serrated
180	0.0019	0.024
178	-0.1052	-0.1827
176	-0.1507	-0.3127
174	-0.3720	-0.4354
172	-0.7065	-0.4885
170	-0.7878	-0.5874
168	-0.7631	-0.5981
166	-0.763	-0.6537
164	-0.844	-0.5797
162	-0.845	-0.591

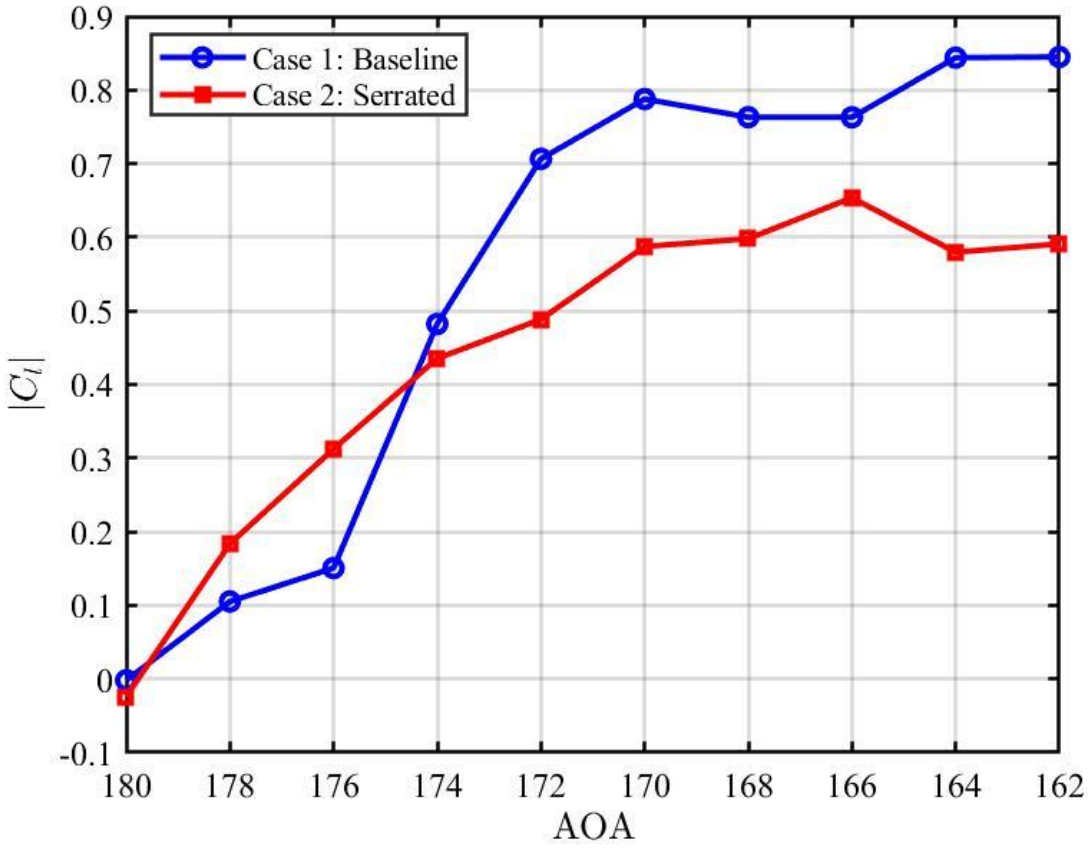

Figure 19:Coefficient of lift: Baseline vs Serrated

5.2 Drag Coefficient

The overall absolute values of the drag coefficients for the baseline and serrated configuration is tabulated in Table 8 and presented in Figure 20. Both blades exhibit nearly identical drag coefficient values at lower static pitch angles, specially from 180 º to 174 º (0 º to 3 º in reverse flow). Noticeable differences in drag coefficient begin to emerge beyond 172 º. Beyond 172 º steep rise in the coefficient of drag is seen in the baseline case. For baseline case, the drag curve follows a quadratic trend up to 168 º. Beyond 168 º the curve transitions into a more linear slope. In contrast the serrated blade case, the drag curve follows quadratic trend for all AOA. In the lift curve, the curve plateaus after 172 º and in drag curve the absolute values for drag coefficient increases rapidly after 172 º. Possible causes for this behavior mentioned, may be in the nature of the separation bubble itself. For static pitch angles below 172 º, the lift-induced components of drag may dominate over other contributions. Beyond 172 º, the influence of lift on drag diminishes, with pressure drag becoming the primary contributor due to the formation of a large, open recirculation zone. The serrated blade closely matches the baseline drag coefficient values up to 172 º, after which it demonstrates significant reduced drag. A significant reduction is observed beyond 170 º. In the baseline case beyond 172 º steep rise in the coefficient of drag is seen in the baseline, whereas gradual increment is observed in the serrated case. The peak value $C_{d_{max}}$ for the serrated airfoil is also compared to the baseline. There is an overall reduction in peak value by approximately 46.6%.

Table 8: Coefficient of Drag : Baseline vs Serrated

AOA	Baseline	Serrated
180	0.0595	0.044
178	0.0606	0.0533
176	0.0616	0.055
174	0.0627	0.0651
172	0.0889	0.08
170	0.1285	0.0977
168	0.18	0.01191
166	0.2531	0.1524
164	0.393	0.1749
162	0.45	0.24

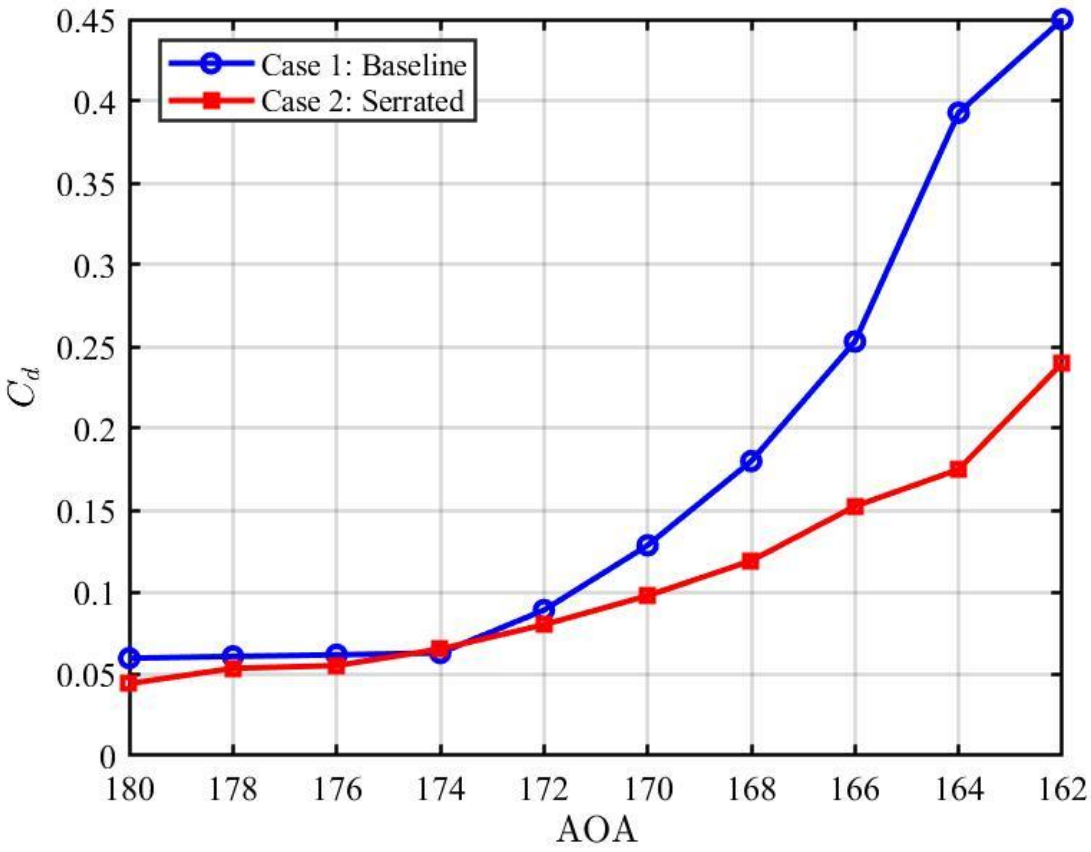

Figure 20:Coefficient of Drag: Baseline vs Serrated

5.3 Comparison with Experimental

The comparative analysis of the lift coefficient for baseline blade for both experimental and computational cases for baseline is illustrated in Figure 21. In both datasets, there is delayed onset of lift, followed by a rapid increase. The significant increase in lift only after certain deviations is discussed in 5.1 Lift Coefficient. This behavior of significant rise of lift coefficient only after a substantial deviation is characteristics of elliptical bodies (A. Lind, 2014). While both cases follow the same general trend, there is noticeable shift in point of initiation. Experimental case shows sharp increase at 178 °. In the computational case it is delayed until 176 °. This is because the trailing edge is sharp, air flowing backward cannot stay attached easily. It separates immediately. Unlike forward flow, which produces lift linearly starting from very low AOA, reverse flow often produces near-zero lift at very small angles because the flow is completely symmetric. Only after the certain deviations large separation bubble is formed. This causes low-pressure region to form, finally generating a pressure difference and measurable lift. So, the lift is generated after the large separation bubble formation. The reverse flow region is potential black box in numerical and computational methods owing to the heavily vertical nature of the flow and in availability of transition

modeling over regions post reattachment (Marilyn Smith, Aerodynamics of airfoils at high and reverse angles of attack, 2011). Following the initial sudden rise phase, both curves exhibit a nearly increase in lift coefficient from 176 º and 168 º, the computational and experimental results show highest degree of correlation. Deviations is observed after 166 º, after 168 º the experimental data begins to plateau and slightly decline, in contrast to experimental, computational predicts a continued rise in lift reaching up to 0.845.

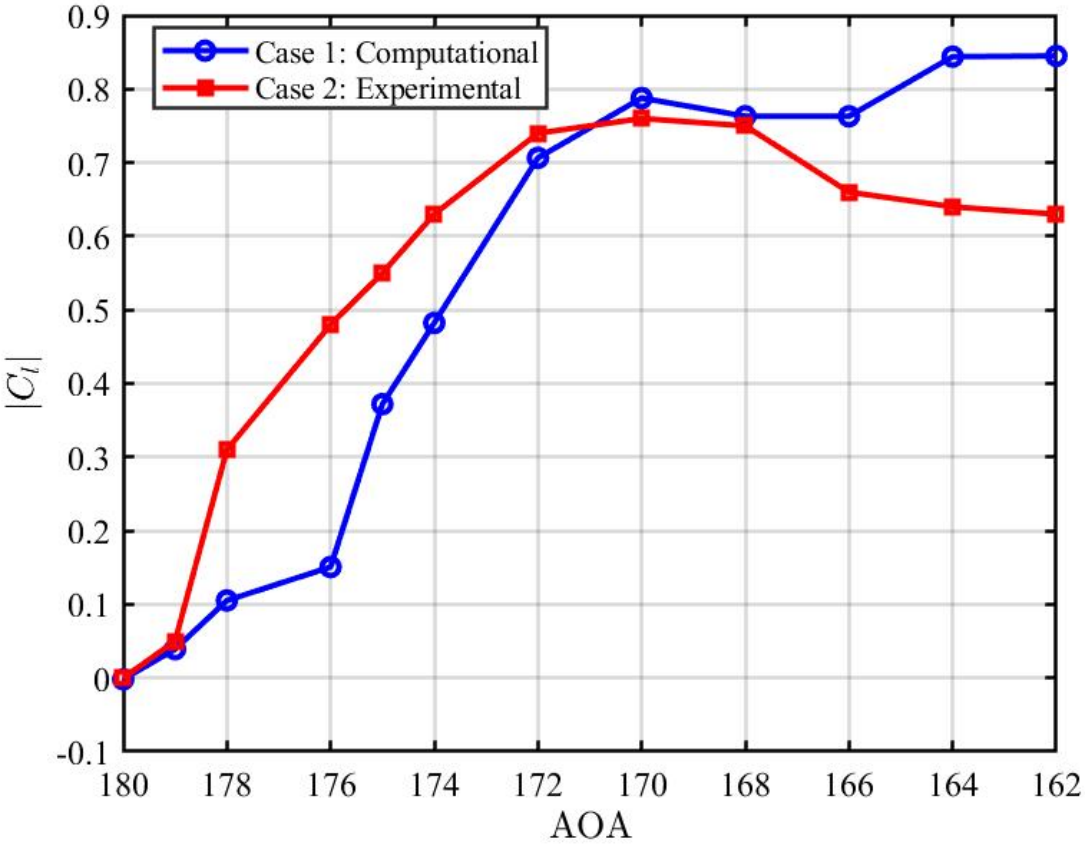

Figure 21: Coefficient of lift: Baseline vs Experimental

The comparative analysis of the drag coefficient blade for both experimental and computational cases for baseline is illustrated in Figure 22. At lower deviations from 180 º to 172 º, both curve show gradual increase in drag. Between 175 º and 168 º, the curves intersect. Up to 168 º, the computational model is actually under-predicting drag slightly or matching it closely. After 168 º, the computational drag skyrockets while the experimental drag increases at a linear rate. This could be because of the blockage effect. Overall the drag gets predicted and the sweet spot is from 175 º to 168 º. If we compare these from lift graph it's actually from the deviation beyond which lift gets generated to the deviation where lift curve gets plateaued. It looks like

the drag is being predicted until it was dominated by lift-induced factor. As the influence of lift on drag diminishes, with pressure drag becoming the primary contributor due to the formation of a large, open recirculation zone the drag is deviated from the experimental values.

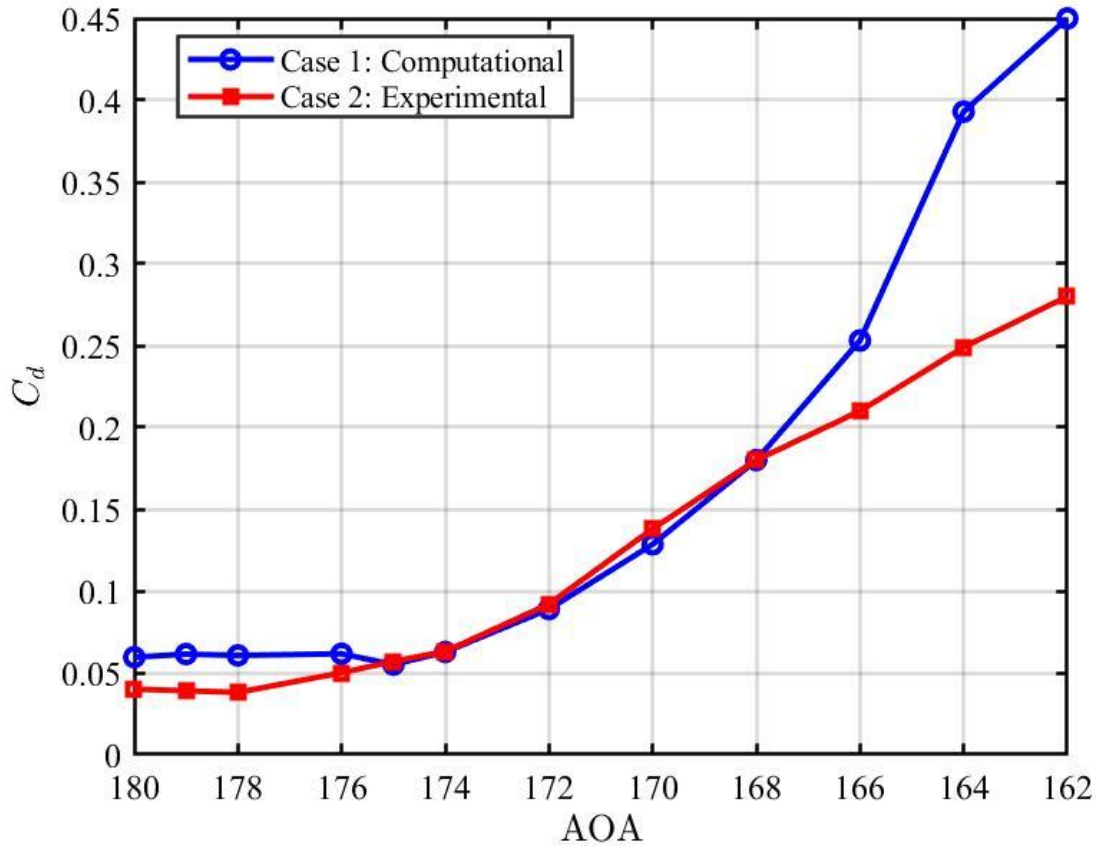

Figure 22: Coefficient of drag: Baseline vs Experimental

The comparative analysis of the lift coefficient for both experimental and computational cases for serrated blade is illustrated in Figure 23. Both experimental and computational show a similar trend, with sudden increase in lift from the initial deviation and increasing linearly up to 170 º. This lift generation from initial AOA is serration acts as vortex generators and they keep the flow attached due to which pressure suction creates lift. A certain plateau is formed after 170 º to 162 º, though a spike in lift coefficient is seen in 166 º in the computational case. The overall phenomenon for computational and experimental cases is similar for the coefficient of lift for the serrated airfoil with computational slightly under predicted lift for almost all cases. The under prediction could be because of the WMLES capability or the wing span. As our wing span is only 20% of chord length which is better at studying quasi-2D effects, It may have played role in under prediction.

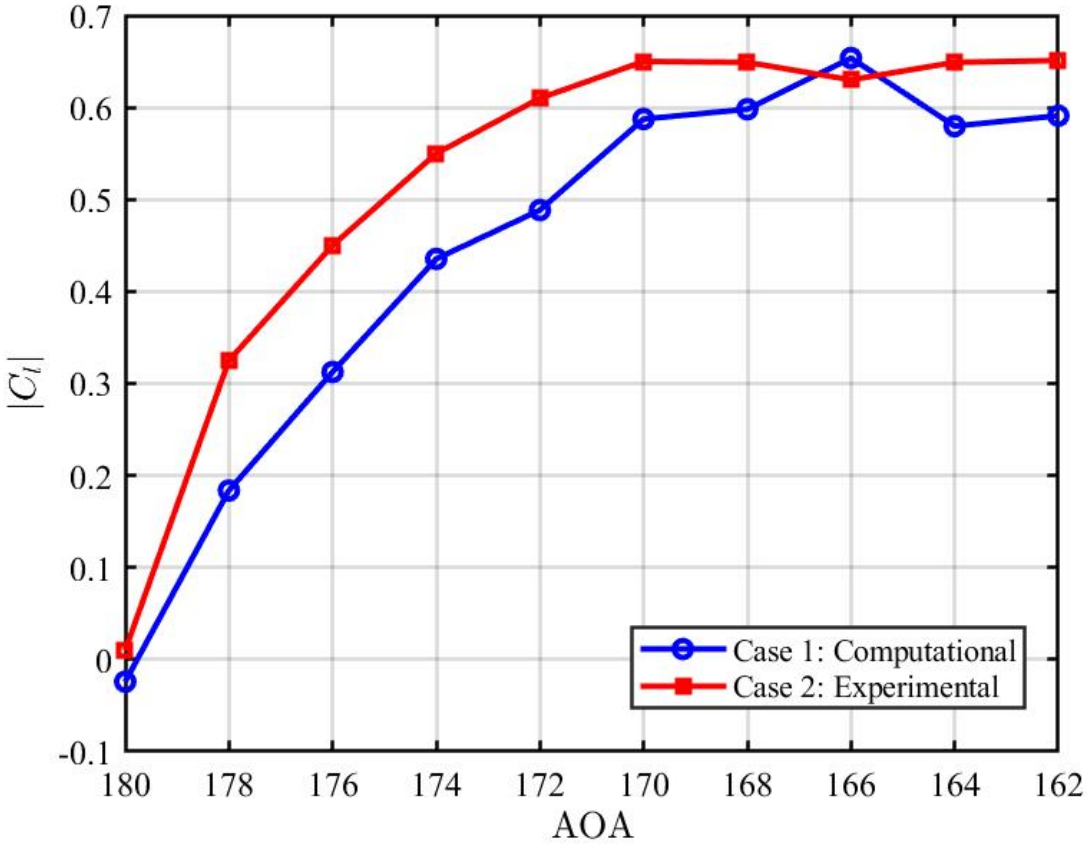

Figure 23: Coefficient of lift: Serrated vs Experimental

The comparative analysis of the drag coefficient for both experimental and computational cases for serrated blade is illustrated in Figure 24. The computational case tracks the experimental case very closely. Both cases show high sensitivity to the deviations. Between 180 ^{o} and 170 ^{o}, the two curves are nearly identical. There is slight deviation between 170 ^{o} and 164 ^{o}, slight over prediction and under prediction. Here, the computational model may be struggling to capture transient flow structures. Overall, the computational case demonstrated a high degree of correlation with experimental results. As in baseline here too, the drag is being predicted until it was dominated by lift-induced factor. As the influence of lift on drag diminishes, with pressure drag becoming the primary contributor due to the formation of a large, open recirculation zone the drag is deviated from the experimental values.

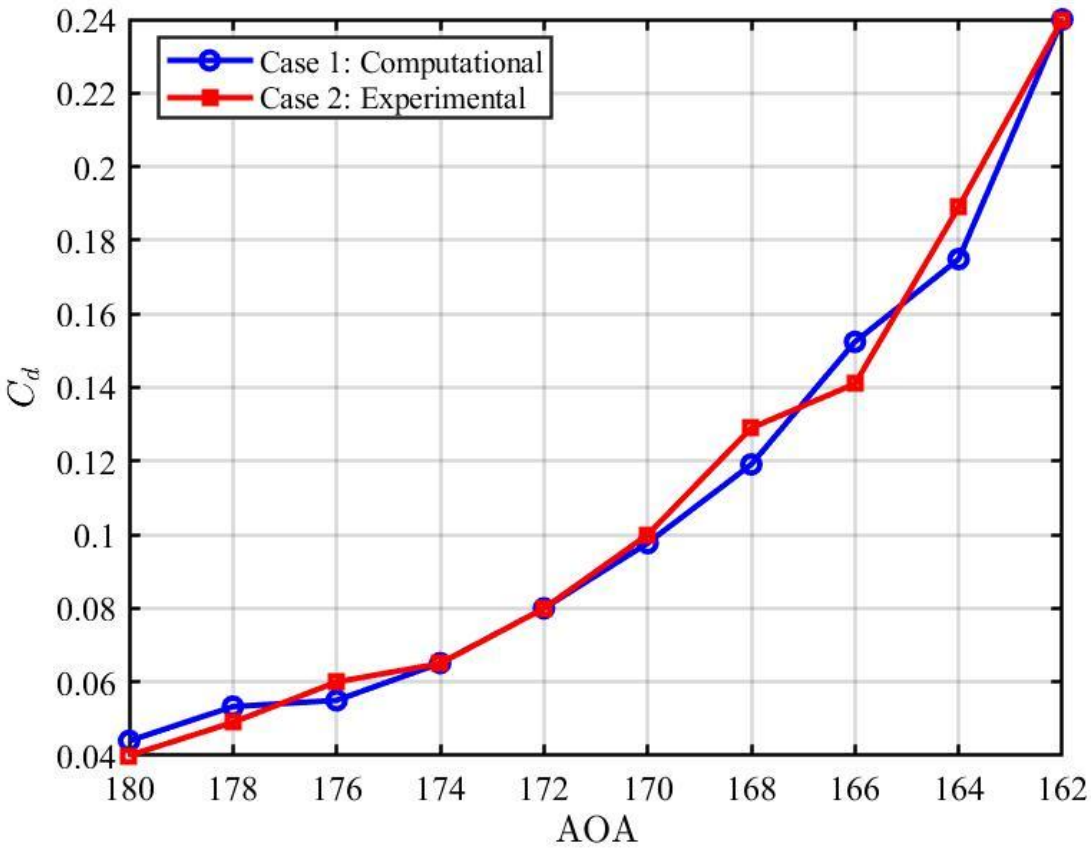

Figure 24: Coefficient of drag: Serrated vs Experimental

5.4 Flow Visualization

5.4.1 Baseline

Contours plots of time-averaged velocity, normalized with free stream velocity of baseline configuration is shown in figures below. The Figure 25 is presented for reference to the grid resolution. The subsequent figures are shown at a relatively smaller scale for comparison.

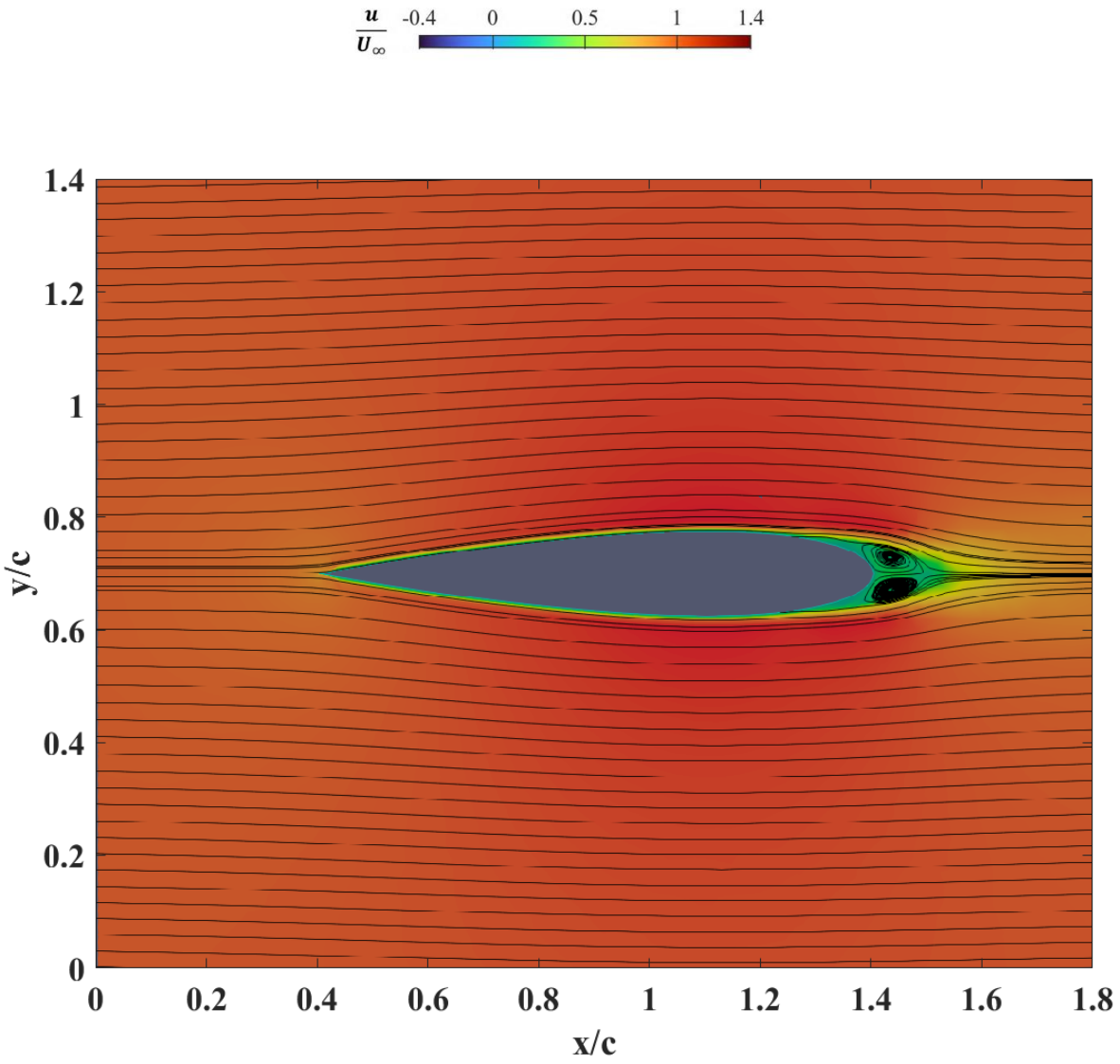

Figure 25: Baseline AOA 180

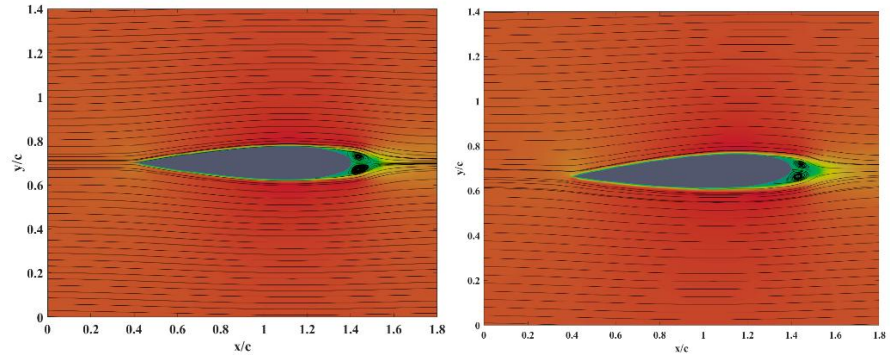

Figure 26: Baseline AOA 180, 178

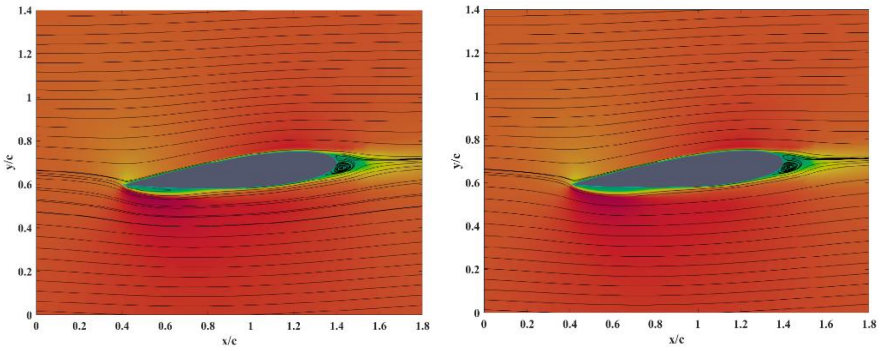

Figure 27: Baseline AOA 176, 174

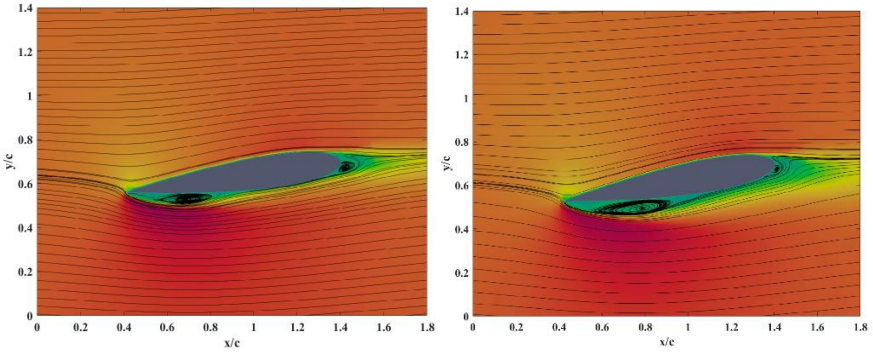

Figure 28: Baseline AOA 172, 170

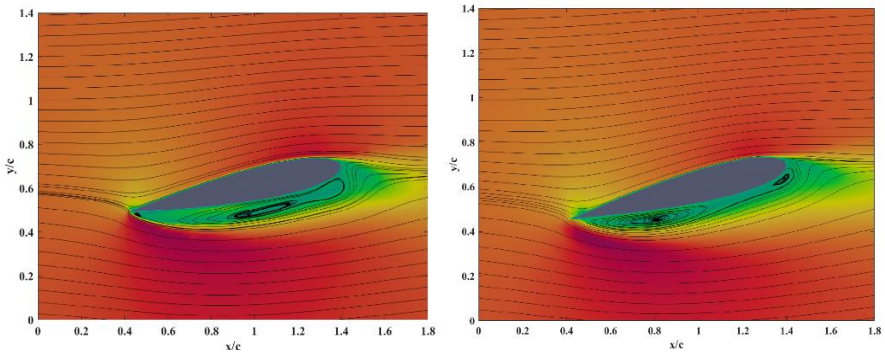

Figure 29: Baseline AOA 168, 166

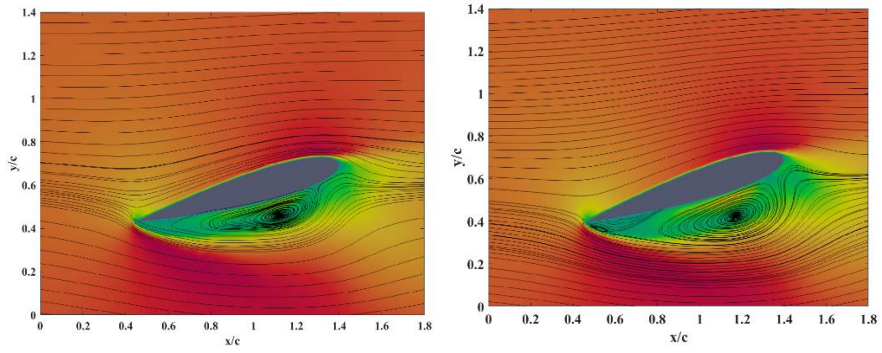

Figure 30: Baseline AOA 164, 162

Each contour plot is overlaid with streamlines of time-averaged velocity to illustrate the flow behavior. The reverse flow region is a potential black-box in numerical and computational

methods owing to the heavily vertical nature of the flow and in availability of transition modeling over regions post reattachment (Marilyn Smith, Aerodynamics of airfoils at high and reverse angles of attack, 2011). For a lower angle of attack, the flow remains attached along the chord. This is observed at 180 º to 178 º. Beyond 178 º, a small circulation bubble starts to appear and grow. The circulation grows in size with increasing angle of attack. The circulation grows in size to approximately 30% of the chord length at 174 º, 50% of the chord length at 172 º and 70% of the chord length at 170 º. Beyond 170 º, the circulation bubble grows to the entire chord length. The flow completely separated from the surface. This corresponds to the significant increase in the coefficient of drag after 170 º in the baseline configuration. Unlike traditional leading edge where flow wraps around smooth curved surface the flow separates earlier. In traditional leading edge the fluid follows the curve due to which it accelerates and lowers pressure. This creates powerful suction right at the front of the wing. This suction peak pulls the wing up, generating most of the lift. But our aerodynamic leading edge is flat surface, the air moving at the high speed cannot wrap around it shoots. This creates separation bubble earlier. Unlike traditional LE, no suction pressure is generated so enough deviations (AOA) have to be reached before the flow on the upper side behaves differently enough from the lower side to produce measurable lift coefficient which can be seen in 176 º.

5.4.1 Serrated

Contour plots of time-averaged velocity, normalized with free stream velocity of serrated configuration at crest, middle and trough position is shown in figures below. The subsequent figures compared to Figure 25 are shown at relatively smaller scale for comparison.

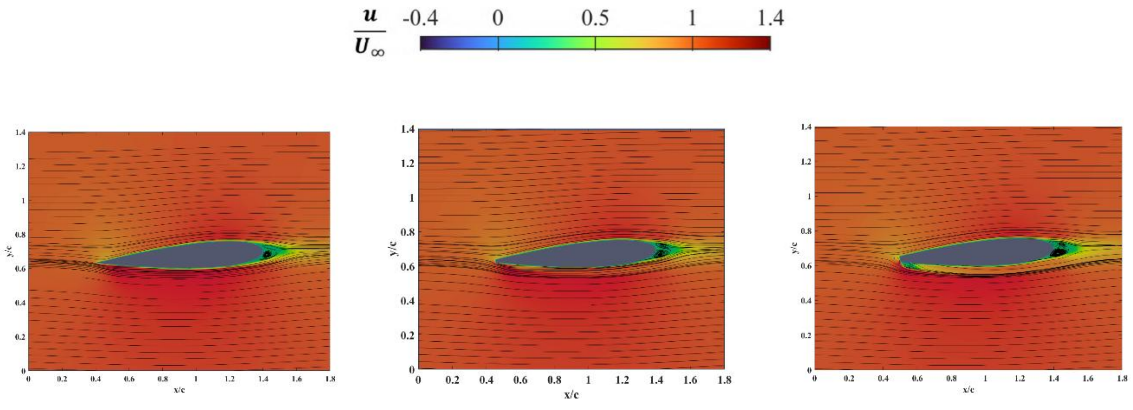

Figure 31: Serrated AOA176: Crest, Middle, Trough

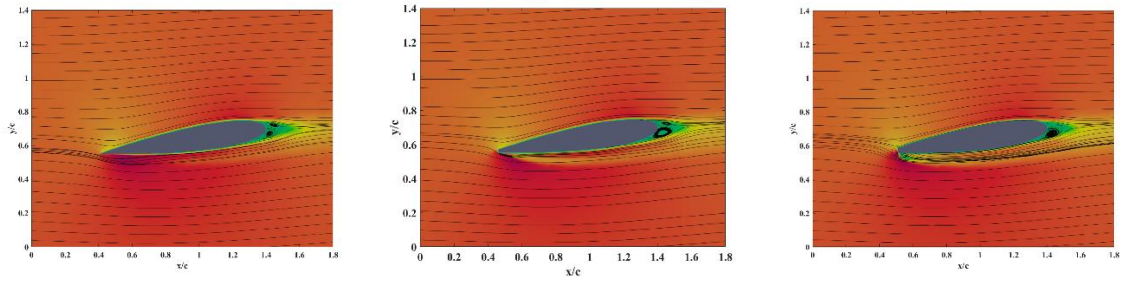

Figure 32: Serrated AOA172: Crest, Middle, Trough

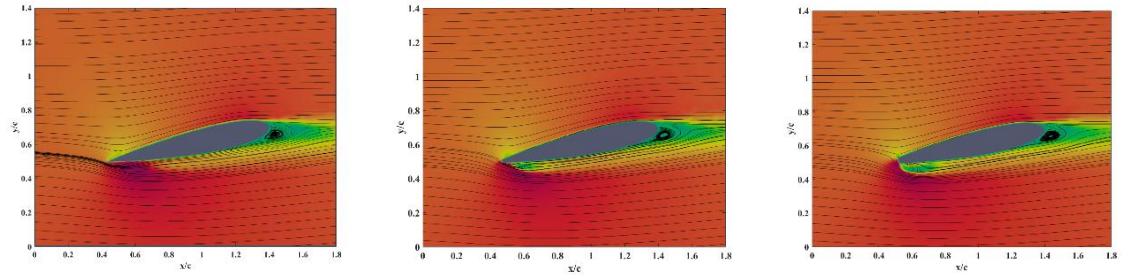

Figure 33: Serrated AOA168: Crest, Middle, Trough

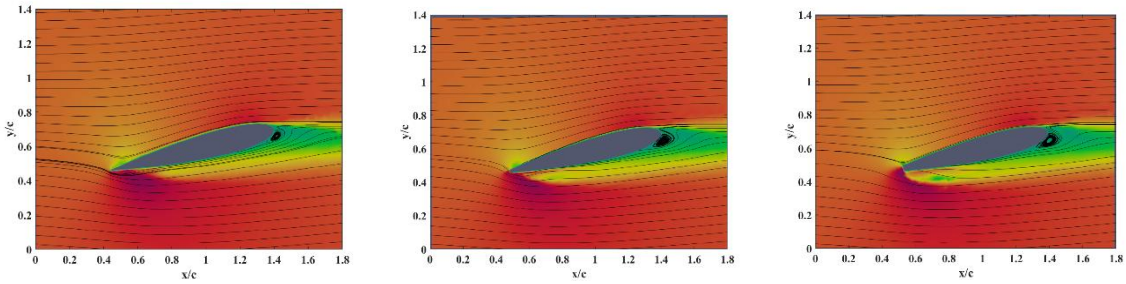

Figure 34: Serrated AOA166: Crest, Middle, Trough

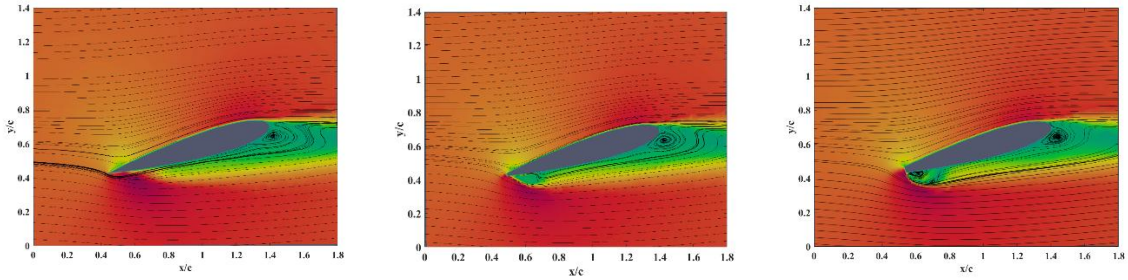

Figure 35: Serrated AOA164: Crest, Middle, Trough

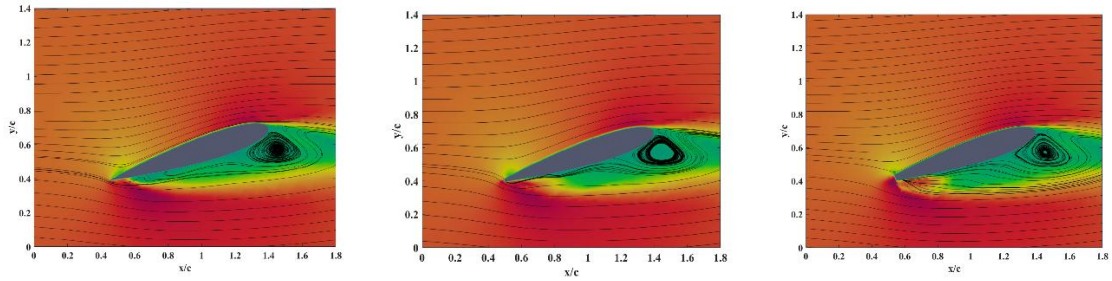

Figure 36: Serrated AOA162: Crest, Middle, Trough

Similar to the baseline case, each contour plot is overlaid with streamlines of time-averaged velocity to illustrate the flow behavior. The analysis focuses on angles of attack 176 º, as flow circulation begins to develop beyond this point. At 176 º, nearly any circulation zone is observed at the crest and middle position, whereas a small circulation region is present in trough position. The flow structure remains largely unchanged up to 172 º. Beyond 168 º, the circulation zone at the aerodynamic trailing edge for all three cross-sections. Additionally, the circulation zone near aerodynamic leading edge becomes more evident in trough cross-section and a circulation zone starts to form in middle cross-section. At 166 º, the circulation zone originating near the aerodynamic trailing edge expands significantly downstream. This is because till now, the flow was attached. The serrations worked, it acted as vortex generators. The serrations forced the air to spin into stream-wise vortices. These vortices pull high-energy air from the free-stream down towards the surface. This helps flow remain attached to the airfoil or reattach sooner than it would on straight edge. This indicated the presence of a favorable pressure gradient. This was for lower AOA but AOA increases the there is turbulent wake and recirculation zone grows upstream to separate from the surface leading to stalled flow conditions. Similarly, at AOA 164 and AOA 162 the circulation zone have grown upstream. This can also be correlated from lift coefficient graph as lift curve plateaus and becomes stable beyond 164 º. Similar phenomenon was seen in experimental where flow separates at reverse 12 º at 90% chord location, which moves to upstream to 70% chord location at reverse 14 º (Raamesh Balasubramani, 2024). In all three cross-sections, attached flow was observed in regions where the baseline showed separation.

Study done in DMAE, Pulchowk Campus, on leading-edge sinusoidal tubercles showed the tubercles postponed stall by 6º, increase lift by 17 % and reduce drag by 12% (Bishowdip Khadka, 2025). Our study showed serrated trailing edge delays flow reversal. So, use of tubercles in leading edge in sections away from hub and use of serrations in trailing edge in

sections near the hub could benefit the aerodynamic characteristics of rotorcraft at high advance ratios.

CHAPTER SIX CONCLUSIONS AND RECOMMENDATIONS

6.1 Conclusions

Based on tasks performed on the basis of objectives, following conclusions are drawn:

- The serrated blade shows better aerodynamic characteristics. The effects of drag mitigation are seen at higher angle of attack. The peak lift caused by reverse flow is reduced by 30% and the peak drag is reduced by 46.6%.
- The serrated blade mitigates flow reversal. Baseline airfoil undergoes early flow separation, 30% of the chord length at reverse 4 ^{o}, 50% of the chord length at reverse 8 ^{o}, 70% of the chord length at reverse 10 ^{o} and 100% beyond reverse 10 ^{o}. In contrast, in serrated blade significant separation is observed beyond reverse 12 ^{o}.
- The wall modeled large eddy simulation is effective to study reverse flow and separation physics.

6.1 Recommendations

Based on this study following recommendations are drawn:

- Investigating different serrations geometries for reverse flow mitigations.
- Investigating the sensitivity of baseline for deviations to find approximate angle of attack where prominent lift starts to generate.

REFERENCES

A. Lind, J. L. (2014). Time-averaged aerodynamics of sharp and blunt trailing edge static airfoils in reverse flow. *AIAA Journal, 52*, 1-18.

BIOMMICRY. (2016). Retrieved 8 4, 2025, from https://biomimicry2016.wordpress.com/2016/04/18/humpback-whales-stall-reduction/

Bishowdip Khadka, L. M. (2025). Experimental Study of leading-edge sinusoidal tubercles on NACA 63215 wing at low reynolds number. Department of Mechanical and Aerospace Engineering.

Cantrell, P. (n.d.). *Retreating Blade Stall*. Retrieved 7 29, 2025, from www.copters.com: https://www.copters.com/aero/retreating.html

Cooper Nelson, T. K. (2024). Control of Reverse Flow over Cantilevered Swept Blades Using Passive Camber Morphing. *AIAA Journal, 62*(4).

D. Dupuy, A. T. (2019). Effect of the Reynolds number on turbulence kinetic energy exchanges in flows with highly varaible fluid properties. *Physics of Fluids, 31*(1).

George Jacobellis, F. G. (2018). Computational and Experimental Investigation of Camber-Morphing Airfoils for Reverse Flow Drag Reduction on High-Speed Rotorcraft. *AHS 74th Annual Forum*, 1-15.

H. Johari, C. H. (2007). Effects of Leading-Edge Protuberances on Airfoil Performance. *AIAA Journal, 45*(11).

Hiremath, N. (2019). Vortical lift on retreating rotor blades at high advance ratios. *Experiments in Fluids*, 60-90.

Johan LARSSON, S. K.-M. (2016). Large eddy simulation with modleld wall-stess: recent progress and fucture directions. *Mechanical Engineering Reviews, 3*(1).

Komal, H. (n.d.). *Helicopter Pilot must know Retreating Blade Stall and its recovery*. Retrieved 7 29, 2025, from meduim: https://medium.com/heli-pilot/helicopter-pilot-must-know-retreating-blade-stall-and-its-recovery-9ea0417ec010

Marilyn Smith, N. L. (2011). Aerodynamics of airfoils at high and reverse angles of attack. *Journal of Aircraft, 48*(6).

Marilyn Smith, N. L. (2012). Aerodynamics of airfoils at high and reverse angles of attack. *Journal of Aircraft*.

Örlü, P. S. (2010). Assessment of direct numerical simulation data for turbulent boundary layers. *Journal of Fluid Mechanics, 659*, 116-126.

Pope, S. B. (2000). *Tirbulent Flows.* Cambrifge University Press.

Raamesh Balasubramani, R. S. (2024). Experimental Study on the Effect of Siinusoidal Trailing Edge for the control of Reverse Flow on High-Speed Rotorcraft. *AIAA Aviation Forum and ASCEND co-located Conference Proceedings.* Las Vegas.

Retreating Blade Stall. (n.d.). Retrieved 7 29, 2025, from skybrary.aero: https://skybrary.aero/articles/retreating-blade-stall

Timofey Mukha, M. L. (2019). A library for Wall - Modeled Large-Eddy Simulation Based on OpenFOAM Technology. *Computer Physics Communications, 239*, 204-224.

W. Yang, B. S. (2012). The effects of span-wise and chord-wise flexibility on the aerodynamic performance of micro flapping-wing. *Chinese Science Bulletin, 57*.

Xiang IA Yang, K. P. (2021). Grid-point and time-step requirements for direct numerical simualtion and large-eddy simualtion. *Physics of Fluid, 33*(1).

Ye Zhou, T. T. (2019). Turbulent mixing and transition criteria of flows induced by hydridynamic instablities. *Physics of Plasmas, 26*.

APPENDIX

WMLES working:

Filtered momentum equation:

$$\frac{\partial \bar{u}_i}{\partial t} + \frac{\partial \bar{u}_i \bar{u}_j}{\partial x_j} = -\frac{\partial \bar{p}}{\partial x_i} + \frac{\partial}{\partial x_j}\left(\tau_{ij}^{sgs} + 2\nu \bar{S}_{ij}\right) \quad i = 1, 2, 3$$

$$\tau_{ij}^{sgs} = \bar{u}_i \bar{u}_j - \overline{u_i u_j}$$ Unknown

So, eddy–viscosity assumption : $\tau_{ij}^{sgs} = 2\nu_{sgs}\bar{S}_{ij}$

Modified momentum equation:

$$\frac{\partial \bar{u}_i}{\partial t} + \frac{\partial \bar{u}_i \bar{u}_j}{\partial x_j} = -\frac{\partial \bar{p}}{\partial x_i} + \frac{\partial}{\partial x_j}\left(2(\nu + \nu_{sgs})\bar{S}_{ij}\right)$$ Unknown

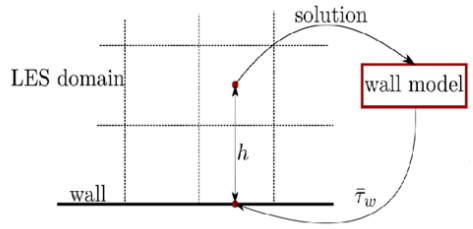

$$u^+ = \frac{1}{\kappa}\ln y^+ + C^+$$

$$u^+ = \frac{u}{u_\tau} \qquad y^+ = \frac{y u_\tau}{\nu}$$

$$u_\tau = \sqrt{\frac{\tau_w}{\rho}}$$

$$\bar{\tau}_{w,i2} = (\nu + \nu_{sgs})_f \frac{\bar{u}_{i,P}}{\Delta x_2}$$

insert

known

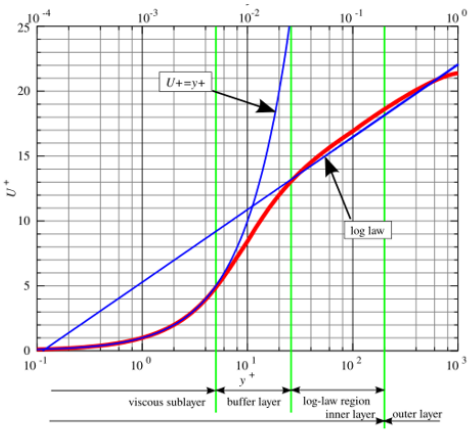

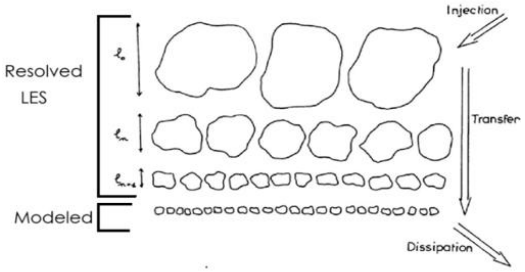

Hardware used:

Architecture:	x86_64
CPU op-mode(s):	32-bit, 64-bit
Address sizes:	46 bits physical, 48 bits virtual
Byte Order:	Little Endian
CPU(s):	32
On-line CPU(s) list:	0-31
Vendor ID:	GenuineIntel
Model name:	Intel(R) Xeon(R) CPU E5-2665 0 @ 2.40GHz
CPU family:	6
Model:	45
Thread(s) per core:	2
Core(s) per socket:	8
Socket(s):	2

This facility is available in Department of Mechanical and Aerospace Engineering, Pulchowk Campus, IOE, TU.

Software section:

Software used: ESI OpenCFD Release OpenFOAM v2412.

The wall model library can be accessed from timofeymukha's github.

Important considerations while setting up the case:

In 0/nut file the sampling index from wall is kept as "1". Index "1" is used to sample from cell center of desired cell.

Wall

{

….

…..

hIsIndex 1

…..

…

}

It's importance can be seen in 0/hsampler file. Here we can give wall-off cell numbers, as 1,2,3…. If 1 is chosen sampling is done from first cell center from wall, if 2 is chosen sampling is done from second cell center from wall and so on.

In 0/hsampler file, we have kept second cell from wall as:

```
wall
 {
      type          fixedValue;
      value         uniform 2;
   }
```

For, temporal validation, adjustable time step is kept with max Co < 0.5.

In pimple loop orthogonal correctors are also used, 4 in precise. We only recommend to use as per your mesh.

त्रिभुवन विश्वविद्यालय
TRIBHUVAN UNIVERSITY
इन्जिनियरिङ्ग अध्ययन संस्थान
INSTITUTE OF ENGINEERING
पुल्चोक क्याम्पस
PULCHOWK CAMPUS
credited by University Grants
mmission (UGC) Nepal 2020
5-521260
5-521611
5-522104
5-522809
पुल्चोक, ललितपुर।
Pulchowk, Lalitpur

Date: May 9, 2026

To Whom It May Concern:

This is to certify that the paper titled "*Wall-Modeled Large Eddy Simulation of Sinusoidal Trailing Edge Impact on Reverse Flow in High-speed Rotorcraft*" (Submission ID #764), with **Biwash Karki** as the first author, was accepted through the peer-review process and has been presented at the 18th IOE Graduate Conference, organized at Pulchowk Campus, Lalitpur, Nepal, from May 7 to 9, 2026.

Please note that inclusion of the accepted manuscript in the conference proceedings is contingent upon timely compliance with any further editorial requirements during the publication process.

Prof. Sangeeta Singh
Convener
18th IOE Graduate Conference

Biwash Karki

WALL-MODELED LARGE EDDY SIMULATION STUDY OF SINUSOIDAL TRAILING EDGE IMPACT ON REVERSE FLOW I...

Tribhuvan University

Document Details

Submission ID
trn:oid:::3117:587924072

Submission Date
May 8, 2026, 3:44 PM GMT+5:45

Download Date
May 8, 2026, 3:48 PM GMT+5:45

File Name
final_draft_Biwash_karki.pdf

File Size
4 MB

51 Pages

7,795 Words

47,818 Characters

6% Overall Similarity

The combined total of all matches, including overlapping sources, for each database.

Filtered from the Report

- Bibliography
- Quoted Text
- Cited Text
- Small Matches (less than 8 words)

Exclusions

- 14 Excluded Matches

Custom Section Exclusions

{titlesCount} Section Titles, {keywordsCount} Keywords

Section title	No. of Section Starters	Section Starters
"Acknowledgements"	4	Acknowledgements, Acknowledgement, Acknowledgment, Acknowledgments

Match Groups

- **41** Not Cited or Quoted 6%
  Matches with neither in-text citation nor quotation marks
- **0** Missing Quotations 0%
  Matches that are still very similar to source material
- **0** Missing Citation 0%
  Matches that have quotation marks, but no in-text citation
- **0** Cited and Quoted 0%
  Matches with in-text citation present, but no quotation marks

Top Sources

5% Internet sources
4% Publications
0% Submitted works (Student Papers)

Integrity Flags

0 Integrity Flags for Review

No suspicious text manipulations found.

Our system's algorithms look deeply at a document for any inconsistencies that would set it apart from a normal submission. If we notice something strange, we flag it for you to review.

A Flag is not necessarily an indicator of a problem. However, we'd recommend you focus your attention there for further review.

Match Groups

- 41 Not Cited or Quoted 6%
  Matches with neither in-text citation nor quotation marks
- 0 Missing Quotations 0%
  Matches that are still very similar to source material
- 0 Missing Citation 0%
  Matches that have quotation marks, but no in-text citation
- 0 Cited and Quoted 0%
  Matches with in-text citation present, but no quotation marks

Top Sources

5% Internet sources
4% Publications
0% Submitted works (Student Papers)

Top Sources

The sources with the highest number of matches within the submission. Overlapping sources will not be displayed.

1	Internet	
core.ac.uk		<1%
2	Internet	
dokumen.pub		<1%
3	Internet	
dspace.rpi.edu		<1%
4	Publication	
Cooper Nelson, Tufan Kumar Guha, Michael Amitay. "Control of Reverse Flow ove...		<1%
5	Internet	
www.researchgate.net		<1%
6	Internet	
d-nb.info		<1%
7	Internet	
www.physicsforums.com		<1%
8	Publication	
Subhajit Roy, Guillermo Araya. "Modal decomposition of compressible ZPG turbul...		<1%
9	Internet	
webthesis.biblio.polito.it		<1%
10	Internet	
spec.org		<1%